



Review article

Design and fabrication of customizable microneedles enabled by 3D printing for biomedical applications

Jia Min Loh^a, Yun Jie Larissa Lim^a, Jin Ting Tay^a, Hui Mei Cheng^b, Hong Liang Tey^{b,c,d,e}, Kun Liang^{a,e,*}

^a A*STAR Skin Research Labs (A*SRL), Agency for Science, Technology and Research (A*STAR), Singapore

^b National Skin Centre (NSC), Singapore

^c Lee Kong Chian School of Medicine, Nanyang Technological University, Singapore

^d Yong Loo Ling School of Medicine, National University of Singapore, Singapore

^e Skin Research Institute of Singapore, Singapore



ARTICLE INFO

Keywords:

Microneedles
3D printing
Drug delivery
Extraction of biological specimen
Biosensing

ABSTRACT

Microneedles (MNs) is an emerging technology that employs needles ranging from 10 to 1000 μm in height, as a minimally invasive technique for various procedures such as therapeutics, disease monitoring and diagnostics. The commonly used method of fabrication, micromolding, has the advantage of scalability, however, micromolding is unable to achieve rapid customizability in dimensions, geometries and architectures, which are the pivotal factors determining the functionality and efficacy of the MNs. 3D printing offers a promising alternative by enabling MN fabrication with high dimensional accuracy required for precise applications, leading to improved performance. Furthermore, enabled by its customizability and one-step process, there is propitious potential for growth for 3D-printed MNs especially in the field of personalized and on-demand medical devices. This review provides an overview of considerations for the key parameters in designing MNs, an introduction on the various 3D-printing techniques for fabricating this new generation of MNs, as well as highlighting the advancements in biomedical applications facilitated by 3D-printed MNs. Lastly, we offer some insights into the future prospects of 3D-printed MNs, specifically its progress towards translation and entry into market.

1. Introduction

Microneedles (MNs) first gained attention in 1998 when Prausnitz's team demonstrated their pioneering work on transdermal drug delivery using solid silicon MNs [1]. As the outermost layer of the epidermis, the stratum corneum serves as a 10 - 20 μm -thick physical barrier that not only prevents unknown substances from entering the skin but also prevents loss of fluid [2] and limits transdermal drug diffusion from the skin [3,4]. They overcame this barrier by pre-treating the skin using silicon MNs, before applying a transdermal patch of calcein, resulting in enhanced drug permeability through the skin by up to four times [1]. MNs consist of an array of needles in the micron scale, usually with heights ranging from 10 to 2000 μm [5] which typically enable access to the epidermis and upper dermis region. MN-based delivery confers many benefits over other common transdermal delivery modalities, including the conventional hypodermic needles and transdermal

patches. Unlike hypodermic needles which directly deliver drugs in bolus form subcutaneously [6,7], MN administration causes minimal pain, low risk of injury due to bleeding and infection, and is easy to perform such that one can potentially self-administer without clinical visitation [8]. In contrast to transdermal patches which can only deliver a limited range of therapeutics with low molecular weights that are able to enter passively through the stratum corneum [9], the penetration of MN into the skin creates passageways that increases skin permeability and grant access of administered therapeutics into deeper skin layers.

MNs are commonly classified into solid MNs, hollow MNs, dissolving MNs, and hydrogel MNs [5,7]. Solid MNs are used to create openings in the skin to enhance the topical permeation of drugs through the skin. Leveraging on the “coat and poke” approach, solid MNs are first coated with a layer of solution containing the drug before inserting the coated MNs into the skin. Hollow MNs, on the other hand, uses a “poke and flow” approach, where the drug is released through the hollow MN channel directly into the skin after MN insertion into the skin. Hollow

Peer review under responsibility of KeAi Communications Co., Ltd.

* Corresponding author. A*STAR Skin Research Labs (A*SRL), Agency for Science, Technology and Research (A*STAR), Singapore.

E-mail address: kun_liang@asrl.a-star.edu.sg (K. Liang).

<https://doi.org/10.1016/j.bioactmat.2023.09.022>

Received 26 June 2023; Received in revised form 22 August 2023; Accepted 30 September 2023

2452-199X/© 2023 The Authors. Publishing services by Elsevier B.V. on behalf of KeAi Communications Co. Ltd. This is an open access article under the CC BY-NC-ND license (<http://creativecommons.org/licenses/by-nc-nd/4.0/>).

Abbreviations			
MN	Microneedles	KOH	Potassium hydroxide
ISF	Interstitial fluid	PCL	Polycaprolactone
HA	Hyaluronic acid	PLGA	Poly(lactic-co-glycolic acid)
PVA	Polyvinyl alcohol	UV	Ultraviolet
PVP	Polyvinylpyrrolidone	PDMS	Polydimethylsiloxane
GelMA	gelatin methacryloyl	PEGDA	Poly(ethylene glycol) diacrylate
PMVE/MA	Polymer of methylvinylether and maleic anhydride	BSA	Bovine serum albumin
3D	Three dimensional	DMD	Digital micromirror device
FDM	Fused deposition modelling	RWM	Round window membrane
MJ	Material jetting	OVA	Ovalbumin
ME	Material extrusion	PAA	Polyacrylic acid
VP	Vat polymerization	AHP-3	Acetyl-hexapeptide-3
SLA	Stereolithography	TYR	Tyrosinase
DLP	Digital light processing	GI	Gastrointestinal
CLIP	Continuous liquid interface production	CSC	Cardiac stem/stomal cells
TPP	Two-photon polymerization	FDA	Food and Drug Administration
PLA	Poly(lactic acid)	QS	Quality systems
CAD	Computer-aided design	CGMP	Current Good Manufacturing Practices
		CAGR	Compound Annual Growth Rate

MNs can also be used for extraction of cutaneous biofluid such as skin interstitial fluid (ISF) through the channels. Dissolving MNs generally deploy the “poke and release” strategy, where encapsulated drugs are released in conjunction with needle dissolution following skin insertion. To prepare dissolving MNs, biocompatible, water-soluble polymers including hyaluronic acid (HA) [10–17], polyvinyl alcohol (PVA) [18, 19], polyvinylpyrrolidone (PVP) [20–23], or a combination of both PVA and PVP [24–27] are often chosen. Lastly, hydrogel MNs comprise of physically or chemically crosslinked polymers such as gelatin methacryloyl (GelMA) [28,29], methacrylated HA [30–33] and silk fibroin [34–36] which do not dissolve upon penetration. Instead, they are designed to absorb or retrieve dermal tissue fluid containing specific biomarkers for analysis or to release loaded drugs into the skin without the MNs dissolving.

From the initial usage of MNs to facilitate the delivery of topical compounds, application of MN has since expanded to include delivery of payloads to specific targets, e.g. vaccines targeting immune cells, diagnostics of skin conditions and biosensing for health and disease monitoring. This is in part due to the increasing recognition of skin as a reservoir with an abundance of biological materials including multiple cell types, biofluids, microbiome, which can be exploited using customized MNs tailored for the intended purpose. As the MN design is critical to its function, it is important to consider and investigate the various parameters to establish the efficacy of MN in a particular application.

1.1. Design considerations of MNs

Several considerations should be taken into account when designing the MN to ensure that it performs its function optimally. Ideally, the MN should be able to penetrate the skin, at a depth that leads to minimal pain and discomfort for the subject, and subsequently achieve its intended objective such as delivery of the active ingredient or biofluid extraction. In this section, we will discuss the parameters of the MNs that not only affects the functionality of MNs but can also be used to improve its efficacy.

Dimension and geometry of the MNs are the most notable parameters that affect the skin penetration of MN [37]. Several parameters of the MN dimensions have to be taken into consideration, namely MN tip diameter, aspect ratio, MN height and needle density [38,39]. Tip diameter affects the force required for skin penetration, where MNs with smaller tip diameter require lesser force to penetrate skin as compared to

MNs with larger tip diameters. Interestingly, the penetration depth is not affected by tip diameter, as the average penetration depth of MNs with different tip diameters were found to be similar with the same maximal displacement of the MNs [40].

Aspect ratio, defined as a ratio of MN height to its base width, affects the ease of insertion and mechanical strength of the MNs [41]. MNs with higher aspect ratio penetrate the skin more easily [41]; however, an increase in aspect ratio by increasing MN height also causes an increase in failure force [42]. On the other hand, decreasing aspect ratio by increasing base width leads to higher mechanical strength of MNs [37, 43]. In spite of that, it is important to note that an excessive decrease in aspect ratio may result in a low penetration depth due to the rapidly widening MN base and poor skin penetration from difficulties in fabricating a sharp tip [37,41]. While studies have shown that shorter MNs may result in inadequate skin penetration [44], Watanabe et al. demonstrated that skin penetration of shorter MNs may be enhanced by employing an applicator to provide a higher insertion speed [45]. Furthermore, Watanabe et al. also showed that while MNs applied with a higher application speed achieved higher skin permeation, there was no increase in observable skin damage, suggesting the possibility of controlling MN application speed to achieve a balance with skin damage. Despite the advantages of using an applicator in improving the efficiency and reproducibility of MN penetration, it is essential to recognize that rigid applicators may not be appropriate for application on a large surface area, particularly on body regions with curvature [46].

Similarly, the height of MNs has to be optimized to control penetration depth required for its designed purpose, such as drug delivery, whilst minimizing pain, bleeding and infection. Increase in MN height was found to be associated with an elevation of pain and risk of drawing blood [47] as a result of deeper penetration into skin tissue [48]. While shorter needles may be favoured, it is important to note that even for MNs of identical heights, skin penetration depth will vary significantly depending on the material composition. For example, MNs fabricated from Gantrez® AN-139, consisting of copolymer of methylvinylether and maleic anhydride (PMVE/MA), with height 600 µm and base width 300 µm had a penetration depth approximately 78% of its total MN height [48], while carboxymethylcellulose pyramidal MNs of with the same height and base width had penetration depth of approximately only 25%–33% of its MN height [37]. Hence the assessment of skin penetration depth is essential in the fabrication of MNs. In addition, the extent of skin irritation or erythema caused by MNs is predominantly influenced by the skin penetration depth [47,49]. Achieving an optimal

MN penetration depth is crucial in upholding MN functionality while minimizing discomfort.

Increasing MN density has the benefit of increasing volume of drug that can be loaded on a single patch [50], but doing so beyond the optimal density decreases MN interspacing and reduces skin insertion efficiency due to a “bed of nails” effect [50,51]. This “bed of nails” effect is caused by dense array of MNs where the needles are placed too close to each other, causing a very high force required for skin penetration [52]. With the same insertion force, skin penetration depth was found to be lower in MN patches of higher density as opposed to patches of lower density due to MN interspacing [50].

Geometry of MNs is another factor that can be exploited to enhance skin penetration, mechanical strength, delivery efficacy and tissue adhesion of MNs. Table 1 summarizes examples of novel MN design structures developed in recent years. Conical [53] and pyramidal [54] MNs have been generally the standard geometries used for MNs. Mechanical strength of pyramidal MNs was found to surpass that of conical MNs with an approximately 2-fold increase in failure force from a simulation model by Lee et al., which was consistent with his team’s experimental results. This could be possibly due to the larger cross-sectional area of pyramidal MNs [37]. New MN geometries have emerged in recent years to enhance penetration of the polymeric MNs such as the “tanto-blade”-inspired design [55]. This “tanto blade”-inspired MNs made use of bevelled tips to enhance skin penetration due to its sharper tips as compared to conical or pyramidal MNs, whilst maintaining a stable structure. Incorporation of “I-beam” geometry, which are commonly used in the construction industry, into hollow silicon MNs had been studied to assess the effectiveness of this geometry in increasing shear strength of MNs [56]. Tests for shear fracture strength showed that “I”-shaped MNs had higher shear fracture strength in the lateral direction as compared to circular-shaped MNs, while shear fracture strength was weaker in the transverse direction. This “I”-shaped geometry may be adapted in applications where there is higher shear fracture force in a certain direction, to prevent breakage of MNs prematurely. Furthermore, it should be noted that mechanical strength of MNs is not only affected by the dimensions or geometry of the MNs, but it can also be affected by the cargo loaded in the MNs. While Raja et al. showed that incorporation of beta sheet induced microparticles significantly improved mechanical strength of silk MNs [57], Park et al. had contrasting results where incorporation of calcein particles diminished the mechanical strength of PLGA MNs [58]. This variance stemmed from

the interfacial compatibility between microparticles and the silk solution in the former study, yielding a composite material with enhanced mechanical strength. Conversely, in the study involving PLGA MNs, calcein particles had poor adhesion with PLGA, resulting in reduced mechanical strength of the PLGA MNs. Ensuring the safety of MNs is of paramount importance, and a critical aspect is maintaining a safety factor at the highest possible level, ideally significantly surpassing 1.0 [58,59]. This safety factor, calculated as the ratio of failure force to insertion force, serves as a safety measure against MN failure and breakage within the skin. It is imperative to ensure that the MNs have sufficient mechanical strength to prevent failure and breakage, especially in cases where the MNs are not designed to break in the skin or are fabricated using non-biodegradable materials.

Apart from enhancing penetration of polymeric MNs, geometry can be used to enhance drug delivery efficacy of the MNs. One form of drug delivery using MNs include coating solid MNs with a layer of drug. Uddin et al. and Caudill et al. have demonstrated the ability of altering MNs designs to enhance the drug loading efficiency by increasing the surface area of MNs using cross-shaped MN design with 4 fins [60], and faceting a square pyramidal MN [61]. MN designs for drug delivery have also been explored for liquid formulations, where the MNs were either designed to facilitate liquid flow or to trap liquid in the MN, a feature that is distinct from the capabilities of standard MN shapes. Bae et al. developed a spectacular MN design which mimics snake fangs for venom injection, whereby the drug spontaneously flows along the grooves of the MN into the skin upon skin penetration [62]. On the other hand, Lim et al. incorporated a microfluidic channel with the MN array, which allows drug solutions to be easily delivered into the MNs [63], while Torrisi et al. fabricated MNs with cavities from stainless steel sheets, where the cavities act as a reservoir to trap liquid solutions [64].

As drug delivery efficiency through coated or hollow MNs can be impeded due to limitations in drug loading capacity and blockage of channels in the skin [65], efforts to deliver drugs incorporated in detachable dissolving MNs have been explored in recent years to ensure that the drug-loaded MN is effectively embedded in the skin during the entire dissolution process. Arrowhead tip MNs designed by Xue et al. were able to detach and be well-embedded in the skin upon shearing with a thumb [66], while the bubbles incorporated in the MN design by Yang et al. created a fracture point for detachment of the MNs in the skin upon shearing, allowing the MNs to remain inserted in the skin [67].

In the recent decade, researchers have widely explored bio-inspired

Table 1
Novel design structures.

Purpose of Design	Microneedle Geometries	References
Enhance mechanical properties		Adapted with permission from Ref. [55]. Adapted with permission from Ref. [56].
Facilitate drug delivery – Liquid transport		Adapted with permission from Ref. [62]. Adapted with permission from Ref. [63]. Adapted with permission from Ref. [64].
Facilitate drug delivery – Coating		Adapted with permission from Ref. [60]. Adapted with permission from Ref. [61].
Facilitate drug delivery - Detachment		Adapted with permission from Ref. [66]. Adapted with permission from Ref. [67].
Bio-inspired MNs		Adapted with permission from Ref. [68]. Adapted with permission from Ref. [82]. Adapted with permission from Ref. [69].

designs to increase tissue adhesion of MNs, with some design inspirations stemming from honey-bee stingers and shark tooth [68,69]. The honeybee-inspired MN has micro-barbs on the surface on the MN, tilted at an angle that allows easy penetration into the skin but difficult removal due to barbs interlocking with the tissue [68]. Increased tissue adhesion of MNs increases drug efficacy as premature removal of MNs from the skin may result in insufficient dosage delivered. Guo et al. has demonstrated that MN designs with increased tissue adhesion are not only useful in increasing delivery efficacy, but also useful in biochemical analysis and motion sensing through his shark tooth-inspired MN design [69]. The multiple functions of this MN array are made possible by incorporating several features into one, such as integrating a “shell” structure for loading of drugs, microfluidics for biochemical analysis and electrocircuits for motion sensing.

Despite the various design considerations that can be altered to achieve the optimal skin penetration depth, one notable challenge in ensuring consistent skin penetration depth during MN application stems from the intrinsic diversity of human skin composition, condition, and thickness across and even within individuals [70]. This could potentially compromise the reliability and efficacy of the intended application such as biosensing and drug delivery. Ripolin et al. demonstrated that the mean MN skin penetration depth in a group of 10 human volunteers varied from 300 μm to 450 μm [46]. Apart from variation in MN skin penetration depth in the same application site across various individuals, Chen et al. illustrated that MN skin penetration could also vary across different anatomical sites [71]. While the posterior auricular and forearm human cadaver skin had high MN penetration rate close to 100%, the skin at the medial thigh and lower abdomen demonstrated lower MN penetration rate of 87% and 78% respectively. Studies have highlighted variations in both stratum corneum [72,73] and epidermis thickness within individuals across different anatomical sites, which could affect the reliability of biosensing or the efficacy of drug delivery due to the discrepancy between the actual and intended skin penetration depth that the MN was designed for. In particular, Egawa et al. showed that 3 different anatomical sites on one extremity have different stratum corneum thickness: 22.6 μm at the volar forearm, 29.3 μm at the back of the hand, and the highest measurement of 173.0 μm on the palm [72]. To mitigate such issues, customizable MNs may be a good solution to achieve the optimal MN skin penetration depth for each individual, maximizing the reliability and efficacy of biosensing and drug delivery.

1.2. Fabrication of MNs

To implement the desired design specifications, many manufacturing methods have been explored, including micromolding, micromaching, lithography and droplet-air blowing and electro-drawing [7]. Among these, micromolding is the most widely adopted. It is a two-step process that firstly utilizes etching or other methods to fabricate the mold, which is subsequently employed as an inverse template for the casting of MNs. While micromolding is efficient in producing standardized MNs reproducibly, the MNs are limited in terms of design complexity and customizability. With the increasing demand for simpler, consistent and low-cost production of intricate MN designs for specific applications, there have been concerted efforts to explore other methods for fabrication.

In recent years, additive manufacturing, or three-dimensional (3D) printing as it is commonly referred to, has been gaining traction as the representative method for on-demand fabrication of various biomedical products including devices, phantoms, prosthetics and implants with customizable designs – to enhance both functionality and personalization. With the increasing interest in such medical devices, research on 3D-printed MNs have also expanded exponentially – including using various 3D printing techniques to implement complex designs, resulting in highly intricate and personalized prototypes. Next, we provide an overview of 3D printing manufacture of MNs from the design perspective. We will first outline the new generation of MNs fabricated using

various 3D printing techniques and then illustrate how these designs contributed to their applications as highlighted in Fig. 1. Lastly, we will offer a perspective on the outlook of MNs in general and how 3D printing may accelerate the progress of MN in clinical translation [74].

2. 3D-printed MNs

There are two main 3D printing approaches used in fabrication of MNs: material deposition and vat polymerization (Fig. 2). The most common examples of material deposition are fused deposition modelling (FDM) and material jetting (MJ). Vat polymerization (VP) is a light-based 3D printing approach used in the fabrication of MNs, which encompasses techniques such as stereolithography (SLA), digital light processing (DLP), continuous liquid interface production (CLIP), and two-photon polymerization (TPP).

The choice of materials plays a pivotal role in determining the 3D-printing fabrication technique to be employed [75]. FDM predominantly employs thermoplastic polymers as its feedstock owing to its heat-dependent deposition mechanism. While polylactic acid (PLA) is favoured for its relatively modest melting point [76], biocompatibility, and degradability through hydrolysis [8], PVA is also a popular option due to its excellent biocompatibility, robust mechanical strength when dry, capacity to transport solute in a gel state post-skin insertion, short-term gel integrity retention, and eventual dissolution and absorption into the skin [77]. In the 3D printing industry, polymeric materials in liquid state and those with low melting points are favoured due to their affordability, lightweight nature, processing versatility, and ability to offer mechanical support. In spite of this, there has been a growing adoption of materials with higher melting points, such as polyetheretherketone (PEEK) and polymethyl methacrylate (PMMA) [78]. On the other hand, the starting materials for VP fabrication, which depends on light-mediated crosslinking, typically comprise of photo-reactive monomers or oligomers, and photoinitiators. In biomedical applications, commercial medical-grade biocompatible resins like Dental LT Clear [79], Castable Resin [53], IP-S photoresist [80,81] are employed within VP fabrication. However, as these commercial resins

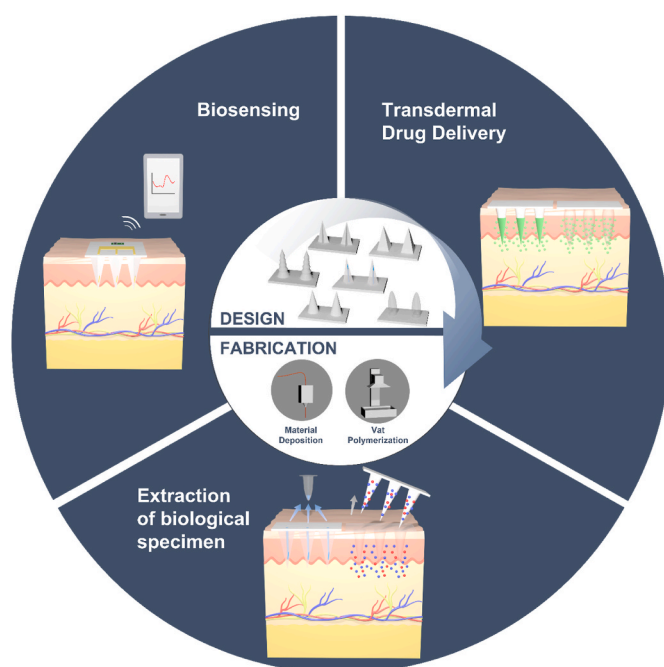


Fig. 1. Schematic diagram showing 3D-printed MNs from conceptualization using computer-aided design designs to fabrication by material deposition and vat polymerization, and subsequently uses in biomedical applications including transdermal drug delivery, extraction of biological specimen and biosensing.

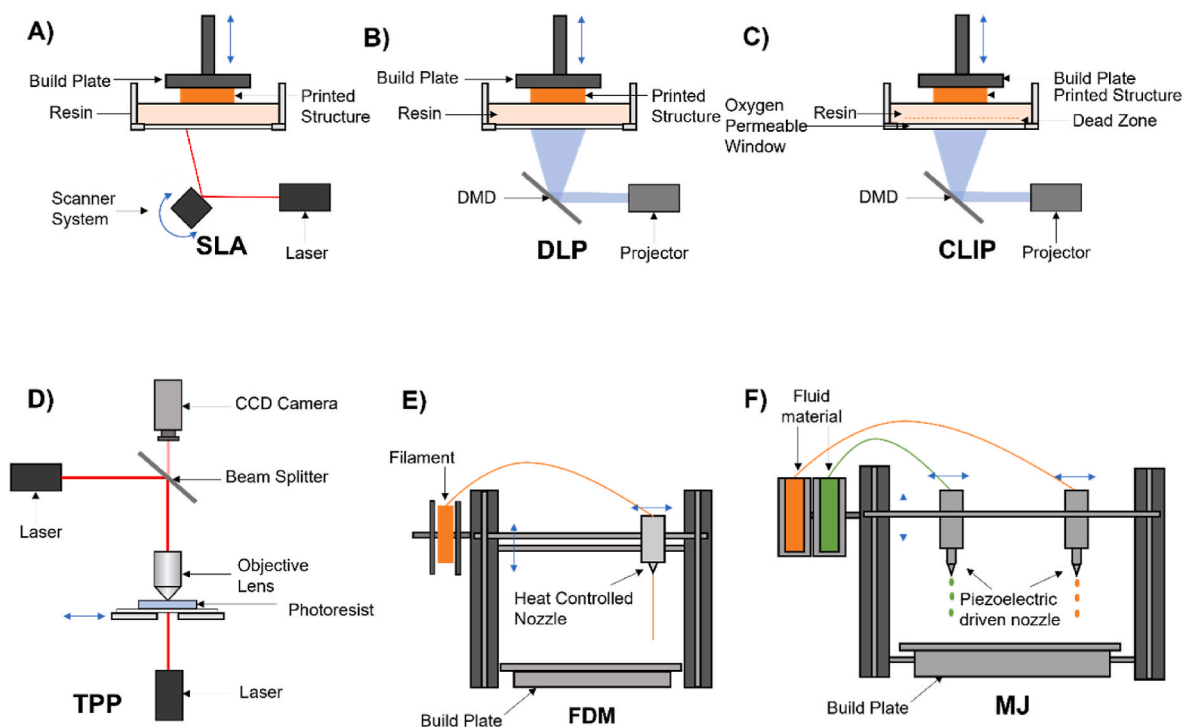


Fig. 2. 3D printing techniques for MNs: (A) Stereolithography (SLA); (B) Digital light processing (DLP); (C) Continuous liquid interface production (CLIP); (D) Two-photon polymerization (TPP); (E) Fused deposition modelling (FDM); (F) Material jetting (MJ).

were not originally formulated with biodegradability in mind, their functionality within biomedical applications may be limited. A number of studies have been conducted on formulation of biocompatible polymers for VP fabrication [34,82,83], allowing for the possibility to incorporate different properties into the printed parts.

2.1. Material deposition

FDM consists of a set of pinch rollers that creates pressure to extrude the molten material [8]. A solid thermoplastic polymer filament is placed into the machine, where it is heated and extruded as a molten polymer by the nozzle of the machine in a layer-by-layer format onto the build plate. Since the next layer is printed before the previous layer fully cools down and solidifies, the two layers fuse. This process repeats until the whole model, designed by computer-aided design (CAD) software, is formed. FDM is the most widespread and affordable material deposition printing method. FDM printers are often favoured in cases where cost is an issue, as FDM printers are cheap and accessible. Although the cost of fabrication by FDM is low, it has a major limitation in terms of low printing resolution. As such, FDM-printed MNs often require a post-fabrication step to improve the resolution of the MNs. Table 2 summarizes the examples of MNs printed using the material deposition technique.

A study by Luzuriaga et al. worked on a post-fabrication process to improve the tip size of the MNs [8]. They attempted to print MNs with a range of shapes, where tip diameter increases from a conical MN to a cylindrical MN. The printer was not only unable to print sharp conical MNs, the tip diameters of the successfully printed MNs range from 170 μm to 220 μm , which are much wider than the optimal tip diameters of MNs (Fig. 3A). With etching for 9 h using 5 M potassium hydroxide (KOH), Luzuriaga et al. reduced the tip size to between 1 μm and 55 μm , which was within the optimal tip diameter range for MNs. In a similar study, Camović et al. printed cylindrical MNs with a FDM printer and chemically etched the MNs using KOH to achieve the desired size and shape that was unachievable by the FDM printer (Fig. 3B) [76]. The etching step decreased the width and the thickness of the printed MNs,

hence achieving MNs with features sufficiently fine for skin penetration with minimal pain [8,76]. While Luzuriaga et al. reported that the FDM MNs were barb-shaped after etching due to the layer-by-layer deposition, Wu et al. suggested that the barb shape of the former's MNs were likely due to inadequate etching [84]. His findings demonstrated that the barb shape could be smoothed with isotropic etching, improving the geometrical structure of FDM-printed MNs (Fig. 3C) which were known for having uneven surfaces due to its layer-by-layer deposition. At present, FDM printers encounter limitations in terms of build speed, precision, and material density. The achievable layer thickness constrains the size and accuracy of the final product. While this limitation can be addressed by employing a smaller nozzle, it results in prolonged building times [85]. Moreover, heat-dependent printers face difficulties in integrating pharmaceutical ingredients into the printing process, as high temperatures could lead to degradation [86]. Nevertheless, Lee et al. has demonstrated the possibility of printing drug-loaded MNs using FDM, although not specifically designed for MNs. They incorporated an antibiotic, rifampicin, into a polycaprolatone (PCL)-based scaffold that was successfully printed using a FDM printer [87]. The incorporation of drug was likely possible due to the choice of thermoplastic with a lower melting point of 60 $^{\circ}\text{C}$, as compared to other polymers such as PLA and poly(lactic-co-glycolic acid) (PLGA) which require extrusion temperature ranging from 190 $^{\circ}\text{C}$ to 230 $^{\circ}\text{C}$ [88], and 175 $^{\circ}\text{C}$ –180 $^{\circ}\text{C}$ [89] respectively. As such, it is important to consider the suitability of excipient polymers in the direct FDM printing of drug-loaded MNs.

Another material deposition method is MJ, which adopts a similar printing method as FDM whereby the prototype is fabricated in a layer-by-layer manner. Unlike FDM, MJ consists of thermal or piezoelectric printheads where liquid building material is deposited dropwise at a high speed [90]. The predominantly used ink for MJ, ultraviolet (UV) curable ink, then requires a short exposure to UV light for curing before deposition for the next layer can proceed. This process is repeated until the whole model is built.

MJ is predominantly favoured for coating the surface of MNs with drugs as opposed to direct fabrication of MNs due to its lower resolution compared to other 3D printing techniques. The dispenser for such

Table 2
Fabrication of Microneedles (MN). Material Deposition – Material extrusion (ME)/material jetting (MJ).

Printing Method	Microneedle Geometry	Microneedle Dimensions	Materials	References
ME	Solid MNs with various configurations (e.g. cone, cylinders with tapered tip, tiered cylinders, cylinder)	Before etching: MN heights: 0.2–2.5 mm MN widths/thicknesses: 0.4–0.6 mm Tip diameters: 0.17–0.22 mm After etching: MN heights: 0.2–2.5 mm MN widths/thicknesses: 0.2–0.3 mm Tip diameters: 0.001–0.055 mm	PLA Filament (Zhunhai Sunlu Industrial Co., LTD)	[8]
ME	Solid MNs in cylindrical configuration	MN 1: ϕ 0.6 x 2 mm MN 2: ϕ 0.465 x 1.45 mm	PLA Filament (Ultimaker)	[76]
ME	Solid MNs in conical configuration after etching, straight and inclined	Before etching (cylindrical structure): MN 1: ϕ 0.7 x 1 mm (straight) MN 2: ϕ 0.7 x 1 mm (inclined) After etching: MN 1 & 2 needle length: 1 mm MN 1 tip diameter: 0.097 \pm 0.021 mm MN 2 tip diameter: 0.086 \pm 0.023 mm	PLA Filament (Mutoh)	[84]
SLA + MJ (Coating)	Inkjet-coated solid MNs (MNs printed by SLA) in flat-spear and square-based pyramidal configuration	Flat-spear MN: 0.08 x 1 x 1 mm Square-pyramidal MN: 1 x 1 x 1 mm	Coating formulations: 1. Insulin:xylylitol (5:1 wt/wt) 2. Insulin:mannitol (5:1 wt/wt) Insulin:trehalose (5:1 wt/wt)	[92]
SLA + MJ (Coating)	Inkjet-coated solid MNs (MNs printed by SLA) in conical and square-based pyramidal configuration	Conical MN: ϕ 1 x 1 mm Square-pyramidal MN: 1 x 1 x 1 mm	Coating formulations: 1. Insulin:xylylitol (5:1 wt/wt) 2. Insulin:mannitol (5:1 wt/wt) Insulin:trehalose (5:1 wt/wt)	[93]
MJ	Solid MNs in square-based pyramidal configuration, with MN tips dispensed by inkjet printing	MN height: 0.5 mm	MN tip: 1. 30% (w/v) Trehalose + 1% PVA 2. 30% (w/v) Trehalose (without PVA) Dye: Congo Red Substrate: 40% (w/v) PVP + 2.5% (v/v) glycerol Veroclear RGD810 (Stratasys)	[91]
MJ	Hollow MNs in triangular-based pyramidal configuration	MN: ϕ (0.5–1.5) x 2 mm Opening diameter: 0.2–0.5 mm	Veroclear RGD810 (Stratasys)	[95]
MJ	Hollow MNs in a triangular-based pyramidal configuration	MN Height: 2 and 3 mm	MNs and backing: Veroclear RGD810 (Stratasys) Ribs between MN islands: Tango Black (Stratasys)	[96]

printers is often piezo-electric driven, where an electric field, originating from the interaction of voltage pulses with a piezoelectric material, causes the nozzle to release a fine droplet in the picolitre range of 1–70 pL [91]. As such, the dosage of drugs coated onto MNs can be accurately controlled in a uniform and reproducible manner. Economidou et al. and Pere et al. reported similar studies where 300 pL of insulin coating formulations were uniformly coated onto SLA-printed MNs using MJ printing without any wastage (Fig. 3D–E) [92,93], while Uddin et al. used MJ printing to coat metal MNs with an anti-cancer drug formulation instead [94]. In another study, Allen et al. incorporated MJ printing into the fabrication of drug-loaded MNs, where piezoelectric dispensing was used to accurately dispense a controlled volume of drug formulation directly into MN polydimethylsiloxane (PDMS) molds (Fig. 3F) [91]. Allen et al. compared a MN with 25 drops of formulation dispensed with another consisting of 100 drops of formulation and the difference in the volume of formulation dispensed was visibly apparent, where the MN with only 25 drops had the formulation localised at the tip while the MN with 100 drops were almost fully filled with the formulation. Material selection remains a significant barrier to MJ production. Currently, commercially available polymers mainly include waxes and photopolymers, with limited availability of printable ceramic and metal

materials. The accuracy of large components produced using MJ is typically inferior to that achieved by other fabrications methods such as VP, primarily because the printing of sizable components necessitates the use of larger droplets for effective printing [85].

One advantage of material deposition that is common to both FDM and MJ is the ability to print with different materials simultaneously due to the availability of multiple print heads, increasing the versatility of MNs printed. A study done by Derakhshandeh et al. used a MJ 3D printer to fabricate hollow MNs with a support material to achieve the high resolution of the MNs (Fig. 3G) [95]. Derakhshandeh et al. drew on the ability to print support structures using sacrificial materials, which are removable by dissolving in chemicals such as sodium hydroxide: a method that grants higher versatility of printing small complex structures where breakaway removal of support structures is not possible. This occurs when the minuscule support structures are used to support the complex structures of individual MNs, or when the support structures are enclosed within the MN structure. Using this advantage of printing with support material, cavities with diameters ranging from 200 to 500 μ m were successfully printed in the MNs. Similarly, Barnum et al. fabricated MNs with cavities using the support material, where the support material removed from the cavities was subsequently replaced

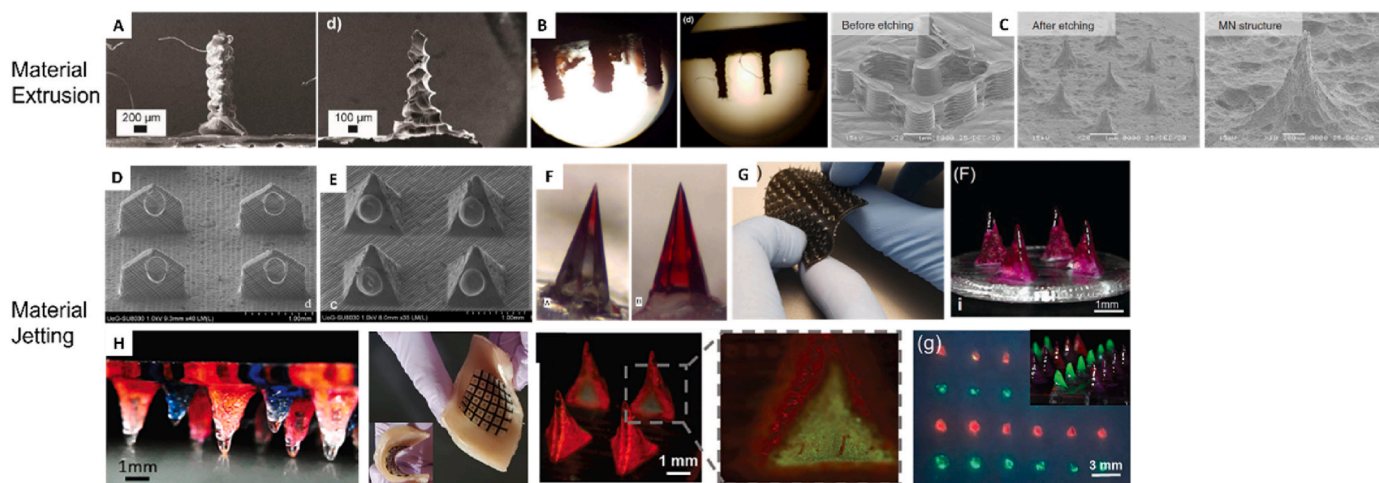


Fig. 3. MNs fabricated with various material deposition 3D-printing techniques. Material Extrusion: (A) SEM images showing effect of chemical etching on reducing FDM-printed MN tip size (Adapted with permission from Ref. [8]). (B) Microscopic images of FDM-printed PLA MNs showing reduced width and thickness of MNs by chemical etching (Adapted with permission from Ref. [76]). (C) SEM images showing straight FDM-printed PLA MNs obtained after chemical etching (Adapted with permission from Ref. [84]). Material Jetting: SEM images of SLA-printed (D) spear-shaped MNs (Adapted with permission from Ref. [92]) and (E) pyramidal MNs (Adapted with permission from Ref. [93]), coated with insulin coating formulations using MJ technique. (F) Microscopic images of MNs with (left) 25 drops and (right) 100 drops of formulation loaded at the tip using piezoelectric dispensing MJ technique (Reproduced with permission from Ref. [91]). (G) MNs printed on a flexible base of a different material using MJ technique; Microscopic view of MJ-printed MNs loaded with red dye (Adapted with permission from Ref. [95]). (H) Hydrogel MNs with different lengths and dyes, printed using material jetting; Image displaying flexibility of the MJ-printed MNs and patch backing in conforming to the bent porcine skin; Fluorescence images showing capability of filling MJ-printed MNs with hydrogels post-printing; Fluorescence image of porcine skin showing deposition of fluorescence by MJ-printed MN array with MNs of different lengths loaded with hydrogels containing different fluorescent markers (Adapted with permission from Ref. [96]).

by model drug-containing hydrogels through pipetting with a special attachment (Fig. 3H) [96]. Barnum's team also demonstrated the versatility of the hydrogel composition by pairing different hydrogels such as alginate and poly(ethylene glycol) diacrylate (PEGDA) with rhodamine B as a model drug, and bovine serum albumin (BSA) protein as a model protein. Not only was the multi-material function used for printing support materials, it was also used to fabricate a sufficiently flexible backing to conform to the skin topography by printing with parts of the backing using a simulated rubber material.

2.2. Vat polymerization

VP is a 3D printing technique that cures photocurable liquid in a vat, in a layer-by-layer process to print a construct [85,97]. The most commonly employed VP techniques include SLA, DLP, CLIP, and TPP, with key differences in terms of the light source and platform repositioning. The high resolution of VP allows rapid fabrication of unique intricate geometries of small structures, making VP printing methods often the top choice for rapid prototyping of intricate biomedical devices such as MNs in recent years [98]. Table 3 summarizes the examples of MNs printed using VP technique.

SLA uses a laser spot that traces the sliced image layer-by-layer on the build platform, after which the build platform raises or lowers slightly for the next layer to be printed. In a study done by Economidou et al., they found that printing at an angle had a significant impact on multiple factors, including the quality of MN and precision of dimensions [99]. MNs were observed to be more blunt when printed at 0° and 90°, with MNs printed at 90° exhibiting noticeable structural defects. However, MNs printed at 45° demonstrated superior sharpness, with no obvious structural defects. In addition, they reported larger dimensional discrepancies detected in the MN tip diameter when printed at different angles and MNs printed at a 45° angle led to the best dimensional accuracy to the nominal CAD dimensions [99]. Although SLA boasts a resolution of 25 μm–140 μm, a study done by Choo et al. has further validated that printing at an angle greatly improves the tip diameter of MNs (Fig. 4A) [100].

Han et al. fully exploited the crosslinking mechanism of SLA to fabricate backward facing barbs on the MNs for increased tissue adhesion, which would have been difficult to achieve accurately with 3D printing as the barbs were not supported by any structure (Fig. 4B) [82]. The triangular backward facing barbs were printed flat using projection microSLA, with one edge connected to the shaft of the MN. This curvature was based on a crosslinking density gradient caused by decay in light intensity projected through the layer, causing the resin at the bottom of the barb to only be partially crosslinked, which was then subsequently removed by washing with ethanol. This created spaces within the crosslinked network at the bottom of the barb, which caused shrinkage as the MN dried, resulting in downward curvature of the barb. With fine control of light exposure and material formulation, layer thickness and crosslinking density of the barbs could be altered to determine the backward curvature of the barbs.

Shrink-molding fabrication has been explored to further enhance the resolution of MNs printed via the VP techniques. This method involves printing a MN master template, which is used to make a negative mold. Hydrogel formulations are then casted into the negative mold to obtain dehydrated or shrunken MNs of the desired shape and size [83,101]. While preservation of the original structure and geometry during shrinking is a concern, Wang et al. has showed that by attaching the base of the hydrogel MN to a polycarbonate film, uniform shrinking of the MN patch is achieved [101]. Interestingly, it was found that for both the conical and pyramidal MNs, contraction rate was higher in the Z-axis. In another study, Ghanbariamin et al. further capitalized the shrink-molding method by first printing the MN master mold using SLA, subsequently using the shrunken hydrogel MNs to make negative molds and repeating this process several times to obtain MNs with increasingly higher resolution [83]. By varying the PEGDA hydrogel concentration, they could tune the rate of shrinkage, MN dimensions and mechanical properties. They also noted a change in the surface topography of the MNs with lower PEGDA concentrations, as evident from the presence of micro-wrinkles [83], likely due to a substantial evaporation of water content from the hydrogel [102].

DLP has a similar working mechanism as SLA, except DLP uses a

Table 3
Fabrication of MNs (VP – SLA/DLP/CLIP/TPP).

Printing Method	Microneedle Geometry	Microneedle Dimensions	Materials	References
SLA	Solid MNs in a pyramidal configuration printed at various printing angles	MN: 0.5 x 0.5 x 1.3 mm	Clear Resin V4 (Formlabs Inc.)	[100]
SLA	Solid MN with cylindrical body and conical tip, with triangular backward facing barbs	MN: ϕ 0.4 x 4 mm Triangular barbs: 0.2 x 0.45 mm	Monomer: PEGDA 250 Photoinitiator (PI): BAPO Photoabsorber (PA): Sudan I	[82]
DLP	Hollow MNs in a conical configuration with 8 microchannels	MN: ϕ 0.3 x 0.5 mm Microchannel: ϕ 0.04 mm	HTL Yellow-5 Resin	[105]
DLP	Solid MNs in a pyramidal configuration	MN: 0.15 x 0.15 x 0.5 mm	Protein: Silk Fibroin PI: 0.5 mM Riboflavin	[34]
CLIP	Solid MNs in a pyramidal configuration with lattice structure	MN: 0.5 x 0.5 x 1.1 mm	Keysplint Hard Resin	[109]
TPP	Solid MN with cylindrical body and conical tip	MN Cylindrical body with tip: ϕ 0.1 x 0.2 mm Taper angle to tip: 9°	IP-S Photoresist (Nanoscribe)	[110]
TPP	Hollow MN with cylindrical body and conical tip with connection to 30G syringe needle	MN: ϕ 0.1 x 0.435 mm MN lumen size: ϕ 0.035 mm	IP-S Photoresist (Nanoscribe)	[81]
TPP	Solid MNs in cylindrical configuration	MN: ϕ (0.63 \pm 0.015) x 6 μ m	IP-DIP Photoresist (Nanoscribe)	[113]
TPP	Open channel MNs with cylindrical body connected to flange-shaped base reservoir	MN height: 700 μ m Open channel diameter: ϕ 30 μ m	IP-S Photoresist (Nanoscribe)	[114]

digital micromirror device (DMD) to project an entire layer instead of spots illuminated by laser beam. This allows the printing process to be much faster than SLA. However, the usage of DMD in DLP to hasten the printing process is not without drawbacks. Firstly, the build size of the printer has an inverse relation with the pixel resolution [103]. In other words, the higher the pixel resolution, the smaller the build size. Also, due to the layer-by-layer printing nature, the surface quality of the print is affected by a stair-stepping effect [104] which can be mitigated by anti-aliasing.

With a high pixel resolution, minute and intricate designs can be printed using DLP printing technique. Using a high precision DLP printer with a pixel resolution of 2 μ m (microArch S130, BMF Material Technology Inc.), Lin et al. successfully incorporated 8 microchannels of diameter 40 μ m into each MN with diameter of 300 μ m (Fig. 4C) [105]. When printing structures with channels, it is imperative to ensure that the MN design and material are able to support skin penetration and does not collapse or break upon application as the presence of channels may result in a weak mechanical structure. DLP has also been used to fabricate hydrogel-based MNs. For instance, Shin and Hyun fabricated a biocompatible protein-based silk fibroin MNs on a flexible substrate using DLP (Fig. 4D) [34]. In this case, a post-printing drying step is required to enhance the mechanical strengths of the MNs. During this

drying process, shrinkage of the hydrogel occurs due to loss of water, which also aided in sharpening of the MN tips [34]. In the study, the natural occurring compound riboflavin (vitamin B2) was chosen as the photoinitiator. While riboflavin is non-cytotoxic [106,107], it is relatively inefficient thus requiring a longer exposure time of 150s for each layer.

With a similar mechanism to DLP, CLIP also prints through projection of UV light. What sets CLIP apart from DLP is the continuous printing process of CLIP, instead of a stepwise layer-by-layer method, allowing CLIP to print faster than DLP by approximately 100 times [108]. An oxygen-permeable window at the bottom of the resin tank allows oxygen, which inhibits photo-polymerization, to constantly permeate through the window to create a “dead zone”. By having this “dead zone”, the printed structure will not be attached to the resin tray and no delamination from the tray is required, hence allowing the printing process to be continuous. Also, by having this continuous printing process, prototypes fabricated from CLIP do not have the stair-stepping effect seen in DLP.

CLIP is a superior choice in printing intricate structures as compared to SLA or DLP techniques due to its continuous printing feature. Rajesh et al. exemplified this by printing highly intricate MNs with a novel design using high-resolution CLIP, with dimensions not replicable by material deposition and features difficult to replicate by SLA and DLP due to the delamination process (Fig. 4E–F) [109]. The square pyramidal MNs have lattice structures made of different lattice shapes such as triangle, tetrahedral, Voronoi, among others. Notably, they fabricated a square pyramidal MNs with triangle lattice shape, where the lattice cell size is 300 μ m and strut size 90 μ m, and another with voronoi lattice shape, where lattice cell size is 350 μ m and strut size 70 μ m. By making use of lattice structures for the bulk of a MN, the amount of material used for printing the product can be greatly reduced. These MNs with lattice structure not only trap liquid for drug delivery (Fig. 4F), but also have the potential to capture ISF in the lattice structure for analysis.

In terms of resolution, TPP is the foremost VP printing technique, which allows fabrication of even more intricate and complex structures. In TPP, two photons are required to initiate polymerization at the intersection of the laser spot [110], where the photoinitiator is excited to produce a free radical which solidifies resin and forms a solid structure [111], allowing pixel resolution to reach up to 100 nm [112]. Aksit et al. perfectly exemplifies the extensive applications of MNs fabricated by TPP, which has feature sizes beyond the abilities of SLA and DLP printing. A single 200 μ m-tall MN with cylindrical body of 50 μ m radius and conical tip with 9° tapered angle was printed for the perforation of guinea pig round window membrane (RWM) (Fig. 4G) [110]. TPP printing enabled an ultra-sharp needle tip with radius of curvature of 500 nm, a sharpness that is practically not achievable by SLA, DLP or CLIP printing due to their pixel resolution. The single MN was printed with a base that could be mounted directly onto a Gauge 23 syringe tip in order to increase the usability of the MN by clinicians. This study manifested the high accuracy and resolution of TPP printing, which extends the use of MNs beyond the scope of skin. Building on this work of perforation of guinea pig RWM, Szeto et al. fabricated a MN using TPP for the sampling of perilymph from RWMs of guinea pigs, overcoming the inaccessibility issue of obtaining cochlear fluid samples due to its location in the inner ear (Fig. 4H) [81]. A single 435 μ m-tall MN with a base to attach to a 30 G stainless steel syringe needle was printed using Photonic Professional GT system. The MN adopted a cone-cylinder stack structure, with a hollow channel for fluid collection. This hollow channel was designed to align close to the centre of the MN body, with the channel opening positioned at the side of the conical tip instead of the centre to retain its ultra-sharp tip. This design achieved a fine balance between mechanical strength and retaining its ultra-sharp tip geometry. Customizability of structures fabricated by TPP were demonstrated when MNs with different geometries were printed using a direct laser writing system (Fig. 4I) [113]. Arrays of triangular-based pyramids, square-based pyramids, cylinders, and conical MNs with

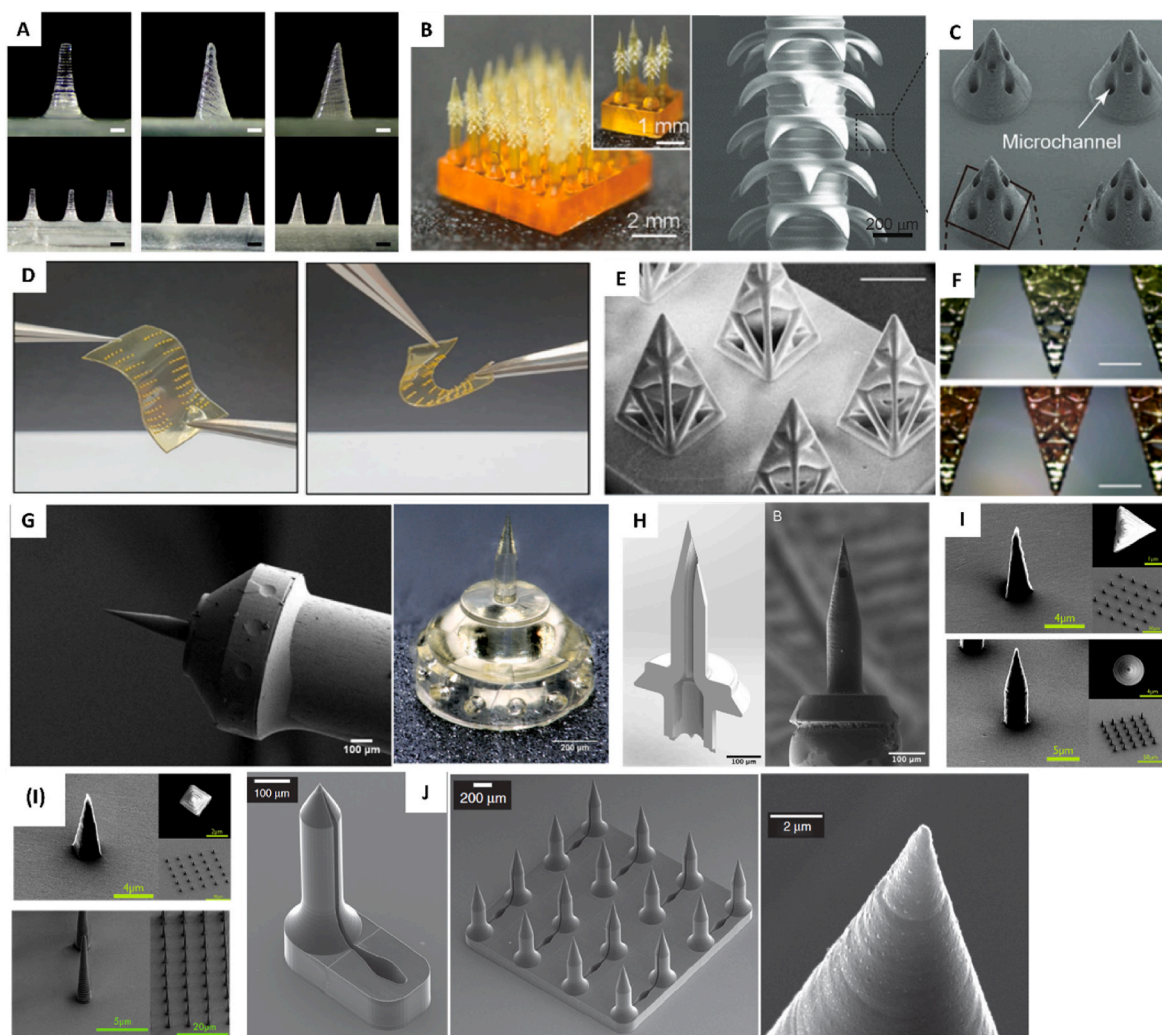


Fig. 4. MNs fabricated with various VP 3D-printing techniques. (A) Stereomicroscope images of SLA-printed MNs, showing improved MN tip diameter with increasing printing angles ranging from 0° to 60° to XY-axes (Reproduced with permission from Ref. [100]). (B) Bio-inspired MNs with backward-facing barbs; SEM image of backward-facing barbs (Adapted with permission from Ref. [82]). (C) SEM image of DLP-printed MNs with 8 microchannels with diameter of $40\ \mu\text{m}$ (Adapted with permission from Ref. [105]). (D) DLP-printed silk fibroin MNs with riboflavin photoinitiator on a flexible backing (Adapted with permission from Ref. [34]). (E) SEM image of CLIP-printed lattice MN patches; (F) Optical images of CLIP-printed lattice MNs after taking up liquid containing food colouring (Adapted with permission from Ref. [109]). (G) SEM image showing TPP-printed MN for perforation of RWM attached onto a 25G syringe tip; Optical image of TPP-printed MN with base for attaching to syringe tip (Adapted with permission from Ref. [110]). (H) CAD rendering showing cross-sectional view of a TPP-printed hollow MN; SEM image of the TPP-printed MN attached to a 30G syringe needle (Reproduced with permission from Ref. [81]). (I) SEM images of TPP-printed MNs and MN arrays with different geometries (Adapted with permission from Ref. [113]). (J) SEM images of TPP-printed MN and MN array with open-microfluidic channels along the body of the MN leading to reservoirs at the MN patch base; SEM image displaying the sharp tip of the TPP-printed MN (Adapted with permission from Ref. [114]).

diameter of $630 \pm 15\ \text{nm}$ and length of $6\ \mu\text{m}$ were printed on a silicon polished substrate. Features in the nanometer scale would have been difficult to achieve even with other VP printing methods.

Nevertheless, the high resolution of TPP comes with trade-offs: high cost and long printing time, which imposes a scalability issue on TPP-printed MNs. As such, TPP-printed MNs are more often used for fabrication of intricate master molds with high resolution. Negative molds of the master molds are casted using silicone elastomer PDMS (SYLGARD™ 184 Silicone Elastomer Kit, DOW), which can be repeatedly used to replicate the master molds, hence increasing the scalability of such intricate structures. However, PDMS negative molds also has its limitations as it is unable to replicate overly complex structures such as lumens or sharp undercuts in MNs due to insufficient structural stability, although moderate undercut angles could still be tolerated [114]. Rad et al. fabricated MN master molds with open-channels using TPP, before casting with PDMS to make negative molds (Fig. 4J). They showed that

the PDMS negative molds could be used repeatedly for at least 22 times without sustaining any damage. It is noteworthy that the dimensions of replicas fabricated using PDMS molds is expected to be smaller than dimensions of the master mold as shrinkage of PDMS increases with increasing curing temperature [115]. Rad et al. found that the PDMS negative mold was smaller than the CAD design by 3.44%, while the replica MN fabricated using PDMS mold was smaller than the CAD design by 3.48% [114]. This shrinkage, however, can be compensated by incorporating the shrinkage ratio into the CAD design of the MN master mold [115], in order to maintain the high resolution of MNs.

Material cytotoxicity and biocompatibility are key concerns of VP fabrication. The widespread use of photoinitiators in this technique emphasized the challenges tied to material toxicity, necessitating the control of photoinitiator concentrations to mitigate potential cytotoxicity effects [116]. To ensure the safety of MN skin applications and to prevent inadvertent injection of excess uncured resins, thorough rinsing

of the MNs is essential. Overall, FDM and MJ fabrication techniques offer versatility and cost-effectiveness in printing, yet they are constrained by their resolution. In contrast, VP fabrication methods deliver high resolution but face limitations concerning cost and versatility [117].

3. Biomedical applications of 3D-Printed MNs

The advent of 3D printing fabrication of MNs in recent years have led to tremendous improvements in their versatility in terms of design, easy customizability and high MN complexity [118]. Not only has this resulted in enhanced drug delivery efficacy of MNs, it also opened up possibilities for new areas of application beyond drug delivery such as the extraction and sensing of biological materials and molecules in the skin microenvironment. To summarize, Table 4 highlights the studies featuring microneedles employed in drug delivery and these new areas of biomedical application.

3.1. Transdermal drug delivery

Owing to the minimally-invasive nature of MNs, they can significantly decrease patient discomfort and pain, as well as reduce the risk of skin trauma and infection which are common adverse reactions associated with hypodermic needles [119–121]. Furthermore, MNs improve the bioavailability of the drug compared to existing methods like transdermal patches and topical formulations [122]. In addition, drug delivery using MNs is a superior choice for some oral medications such as proteins, antibodies, antigens and other bioactive compounds as these drugs were reported to have sub-optimal drug absorption efficiency [123] and could be subject to degradation [124] in the gastrointestinal tract. Conventional MN fabrication methods such as drawing lithography, droplet-air blowing, and electro-drawing are limited in terms of tuneable drug release, poor drug loading and suboptimal efficacy. With the advantage of customizability in the formulation and geometry of MN designs, 3D printing have been exploited to improve these issues. For example, 3D printing enables the precise fabrication of intricate microneedle structures that can accommodate different mechanisms of drug release. Solid MNs fabricated by VP and material deposition techniques can be coated with drugs and released into the skin through passive release [60,61,92], or used for pre-treatment for the poke and patch method, delivering drugs through diffusion [98]. On the other hand, hollow MN, which are usually printed by VP techniques due to its superior resolution, often deliver drugs through the injection method [125,126]. Hydrogel MNs have been fabricated by both VP and material deposition techniques to encapsulate drugs in the MNs for passive release [96,127]. Leveraging the versatility of 3D-printing techniques, 3D-printed MNs can be designed to integrate features to enable the active release of drugs in response to external stimuli such as temperature and pH [128]. As such, 3D-printed MNs have gained interest as a viable option for delivery of drugs in various treatments, including insulin drug delivery [93], anticancer treatment [60] and treatment for topical infections [129].

Drug delivery via MNs offers the advantage of bypassing the stratum corneum, thereby enhancing skin permeability to drugs and facilitating a more efficient transdermal drug delivery [43]. Samandari et al. conducted a study comparing the efficacy of delivering vascular endothelial growth factor (VEGF) through MNs and topical application using a full-thickness wound model in swine [130]. The wound treated by the FDM-printed MNs delivering VEGF demonstrated a noteworthy ability in mitigating excessive wound contraction in contrast to the control groups which consisted of wounds treated with MN-delivered PBS or left untreated. Although wound contraction is required in wound healing, excessive wound contraction is undesirable as it could result in hypertrophic scars [131,132]. Moreover, the granulated tissue within the wound treated with VEGF-delivering MNs exhibited significantly increased vascularization in comparison to the wound treated with

topical delivery [130], highlighting the superior effectiveness of MNs in transdermal drug delivery.

To investigate drug release profiles of MNs with different geometries, Pere et al. fabricated solid conical and pyramidal MNs with a height of 1 mm using SLA [93]. Bovine insulin-sugar films were then coated on the surface of the MNs using MJ, with approximately 350 µg of insulin per array. Although the cone configuration displayed better skin penetration abilities, the drug release profiles for both configurations were comparable. Another similar study was conducted by Economidou et al. using spear and pyramid MN configurations [92]. The pyramid configuration displayed better drug release rates than the spear configuration as it has a larger exposed surface area for hydration of the solid drug coating to take place which therefore enabled dissolution of the drug to occur at a faster rate. In addition, the pyramid configuration also demonstrated better skin penetration capabilities than the spear configuration.

One common challenge of MN-based drug delivery is the limited drug loading capacity. To improve the drug loading capacity of the MNs, Uddin et al. fabricated cross-shaped MNs with SLA and coated them with cisplatin-polymeric layers via MJ, for usage in anticancer treatment (Fig. 5A) [60]. The cross-shaped design could allow up to 7.0 mg of coated material to be loaded onto the MNs, compared to existing MN designs which can only accommodate up to a few milligrams of coated material. The MNs also demonstrated good skin penetration abilities and were able to successfully penetrate the stratum corneum by applying just 3 N of force. In addition to increasing the drug loading capacity of the MNs, having a cross-shaped geometry can also help to facilitate wound healing and hold the skin together [129]. Similarly, to improve drug loading capacity, faceted MNs with horizontal grooves were printed by Caudill et al. using CLIP, which was dip-coated into a CLIP-printed coating mask loaded with ovalbumin (OVA) and CpG (Fig. 5B) [61]. As compared with square pyramidal MNs, OVA drug loading was 36% higher in the faceted MNs which could be attributed to a thick drug coating due to its geometry features since theoretical increase in drug loading capacity of the faceted MNs was only 21.3%. The faceted MNs also demonstrated great potential in vaccination applications as a 50 times higher OVA-specific IgG response was induced in mice on day 30 after a booster immunization was administered on day 23, as compared with subcutaneous or intradermal injection methods (Fig. 5C).

The drug release profile of MNs can also be improved by spatial configuration of the drug during the additive manufacturing process. Using CLIP, Johnson et al. fabricated Janus MNs to localise the loaded drug to a water-soluble tip. The Janus MNs which consist of a hydrophobic poly-ε-caprolactone trimethacrylate (PCL-tMa) base, and a hydrophilic polyacrylic acid (PAA) tip with 0.05 wt% of rhodamine B (surrogate drug) (Fig. 5D). When tested ex vivo on murine skin, the Janus MNs were able to dissolve entirely in the skin and completely release the surrogate drug, thereby demonstrating that localisation of the drug to the tip does improve drug delivery (Fig. 5E–F) [133].

In addition to optimising the geometrical configurations of the MNs, 3D printing can be leveraged to manufacture personalized MNs to accommodate the irregular topology of skin contours. Lim et al., fabricated personalized MN patches with different curvatures using DLP for transdermal delivery of an anti-wrinkle small peptide, acetyl-hexapeptide-3 (AHP-3) (Fig. 5G) [98]. A commercial resin - 3DM-castable resin from 3D-Materials SASU (Feldkirch, France) was chosen for MN manufacture. Using calcein dye as a surrogate of AHP-3, they demonstrated that pre-treatment with personalized MN patches not only achieved the highest permeation of calcein dye over 18 h in human cadaver dermatomed skin, but also had the deepest penetration depth of approximately 750 µm, as compared with flat MN patches and non-treated skin with penetration depth of approximately 480 µm and 220 µm respectively (Fig. 5H–K). Using AHP-3, the personalized MN patches had enhanced cumulative permeation of approximately 45 times across the human cadaver skin after 24h, in comparison with flat MN patches. However, mechanical testing revealed that the mechanical strength of the commercial resin was insufficient, as compression testing

Table 4
Applications for 3D printed microneedles.

Sample Drug	Fabrication Method	Microneedle Characteristics	Method of Delivery	Type of Efficacy Studies	Experimental Outcome/Results	References
Drug Delivery						
Insulin	SLA + Inkjet printing (coating)	Solid-coated, pyramid and conical designs	Coat and poke	In vitro studies using dermatomed porcine skin	90–95% of loaded insulin released from MNs after 30 min	[93]
Insulin	SLA + Inkjet printing (coating)	Solid-coated, pyramid design	Coat and poke	In vitro studies using abdominal porcine skin In vivo studies using diabetes-induced mice	In vitro: 80% of loaded insulin released within 2 min, 86–92% released within 8 min In vivo: Plasma blood glucose level decreased by ~30.1% after 1h	[92]
Cisplatin	SLA + Inkjet printing (coating)	Solid-coated, cross-shaped design	Coat and poke	In vivo studies using BALB/c nude mice inoculated with A431-human squamous carcinoma cells	90–100% of loaded cisplatin was released within 1h after application, and significant growth control of cancer cells observed when MNs were applied to non-tumour sites	[60]
Zinc oxide and nanocrystalline silver	Visible light dynamic mask micro-SLA + Pulsed laser deposition (coating)	Solid-coated, cross-shaped design	Coat and poke	24 h agar diffusion assays	Silver-coated arrays produced zone voids of growth and zinc oxide-coated arrays produced zones of inhibited/reduced growth when tested against <i>Staphylococcus aureus</i> and <i>Staphylococcus epidermidis</i>	[129]
Ovalbumin and CpG	CLIP	Solid-coated, faceted design	Coat and poke	In vivo studies using C57BL/6 mice	OVA-specific IgG response on day 21 and day 30 (boost immunization was given on day 23) was 20 times and 50 times higher, respectively, in MN vaccinated mice compared to SC and intradermal injected mice.	[61]
Rhodamine B	CLIP	Solid dissolving MNs	Diffusion	Ex vivo studies using murine skin	MN tips containing rhodamine B were observed to have completely dissolved in the skin.	[133]
Acetyl-hexapeptide-3 (AHP-3)	DLP	Solid conical MNs on a personalized patch	Poke and patch	In vitro studies using dermatomed human cadaver skin	Cumulative skin permeation of AHP-3 was 45 times higher in skin treated by personalized MN patch as compared with flat MN patch.	[98]
Acetyl-hexapeptide-3 (AHP-3)	DLP	Hydrogel, Personalized MN patch		Drug release and recovery study in PBS	The photopolymer combination of 70% VP and 30% PEGDA had higher change in weight over 8h than other photopolymer combinations, signifying higher rate and extent of drug release.	[51]
Red, green and blue fluorescence: rhodamine B, fluorescein isothiocyanate and methylene blue respectively	SLA	Hollow MNs with internal microfluidic channels	Poke and flow	Ex vivo studies using porcine skin	Fluorescence image intensities showed fluorochrome skin penetration ranging between 100 and 200 μm . Confocal imaging of porcine skin injected with fluorochromes with varying flow rates demonstrated effective control of drug input.	[79]
Fluorescein	TPP	Solid MNs with open microfluidic channels	Poke and flow	In vivo studies using euthanized rabbit ear	Fluorescein solution delivered by the MNs reached at least 160 μm , at least 2 times deeper than delivery without MNs at 66 μm , signifying more effective delivery of drugs into skin using the MNs.	[114]
Cy5 (model drug)	MJ	3D-printed microheater attached to micromolded MNs	Diffusion	In vitro studies using cadaver rat skin	Wider and more intense fluorescence signals was exhibited from MN with microheater group as compared with MN only group, suggesting enhanced drug release due to heat from microheater.	[134]
BSA	DLP	Hollow MNs integrated with ultrasound function	Poke and flow	In vitro studies using porcine skin	Penetration of BSA delivered by ultrasonic MNs and by MNs only was 24 times and 9 times, respectively, compared with delivery by passive diffusion.	[126]
Rhodamine B (model drug)	Projection Micro-SLA	Barbed MN arrays	Diffusion	In vitro studies using chicken breast skin-barrier model	Barbed MNs were able to release ~2.5 μg of rhodamine B continuously for 6h in chicken breast skin-barrier model	[82]
Sample Extraction						
CRP and PCT in ISF	SLA	Hollow MNs	Passive flow (uptake)	Ex vivo studies using porcine skin	Surface modified MNs with PEGylation were able to complete the lateral flow assay in 5 min while non-PEGylated MNs could not.	[148]

(continued on next page)

Table 4 (continued)

Sample Drug	Fabrication Method	Microneedle Characteristics	Method of Delivery	Type of Efficacy Studies	Experimental Outcome/Results	References
Fungal species	DLP	Solid MNs	Poke and remove	Human studies	Sampling of scalp by MNs had greater fungal diversity compared with swab and tape strip.	[149]
Perilymph sampling	TPP	Hollow MN	Ultra Micro Pump	In situ studies using juvenile guinea pigs	1 μL of perilymph was extracted from the cochlea over 45s without causing long-lasting damage to hearing or RWM.	[81]
Colon cancer cells	TPP	Solid MNs	Cell seeding and culture on MNs	In vitro studies using HCT 116 colorectal carcinoma cells	Cells were viable and were observed to envelop itself around MNs, indicating a good interaction with MNs.	[113]
Biosensing						
Potassium ions	TPP	Conical-shaped hollow MNs	Electrochemical Sensing	Bench-top studies using potentiostat	Porous carbon K + ISE integrated into a fluidic chip, was able to measure potassium concentration in a range of 10^{-5} to 10^{-2} M with a rapid stabilization time of ~ 20 s, using a hollow MN.	[155]
Tyrosinase	DLP	Triangular-based hollow pyramid-shaped MNs	Electrochemical Sensing	Ex vivo study using porcine skin	Larger current signals were recorded for porcine skin with increasing concentration of TYR as compared with TYR-free porcine skin with no current signal recorded.	[154]
H ₂ O ₂	TPP	Conical-shaped solid MNs	Electrochemical sensing	In vivo studies using diabetic mice	Blood glucose concentration measured using the MN biosensing device corroborated well with measurements from a commercial blood glucose meter.	[160]

rendered substantial damage to MNs across the 3 curvatures, with the number of MNs damaged varying from 2% to 52%. To improve the mechanical strength of the MNs, the authors repeated the experiment using 3D printed MN patches based on PEGDA and PVP [51] and found that the percentage of MNs that remained intact after application was more than 98%.

3D printing also enables the design and fabrication of highly intricate and complex MN to enhance drug delivery efficacy. Yeung et al. fabricated hollow MNs microfluidic-enabled hollow MNs from a Class IIa biocompatible resin (Formlabs, Dental LT Clear) using SLA (Formlabs, Form 2) (Fig. 5L) [79]. The incorporation of the microfluidic channel into the MN allows for rapid and controlled transdermal delivery of drugs. Furthermore, the device can also be used to facilitate homogeneous mixing of multiple fluids under different flow rates, as well as the transdermal drug delivery of the fluid mixture. Similarly, Rad et al. used TPP technique to fabricate a high-resolution MN array with open microfluidic channels along the MN shaft and the MN patch (Fig. 5M) [114]. The design of this MN array taps on the capillary action mechanism for loading of the reservoir upon dipping the MNs into a liquid solution, whereby solution flows through the open channels along the MN shaft into the reservoir at the patch base. Fluorescein solution was used to check the solution penetration depth by the MN array. Fluorescein delivered using the MN array penetrated at least 160 μm deep into the cadaveric rabbit ear (Fig. 5N), compared to only 66 μm when directly applied (Fig. 5O). The fluorescein signals were also observed to have diffused well into the surrounding area after 3 h (Fig. 5P).

The incorporation of a heating element in MN has also been explored via 3D printing [134]. Using MJ printing, Yin et al. developed a microheater drug-encapsulated MN patch system made from an ink solution comprising of PDMS and multiwalled carbon nanotubes (MWCNTs) (Fig. 5Q). By increasing the temperature at the skin application site, the presence of the microheater in the MN device speeds up the dissolving rate of the MNs, resulting in an increased rate of drug release and diffusion (Fig. 5R). Due to its rapid rate of drug release, this MN device has the potential to be used in delivery of analgesics for pain relief. Apart from incorporating a microheater to enhance drug release, sonophoresis incorporated with MNs can be another method to enhance drug delivery through the skin by generating not only heat, but also a

fluid force that propels drug diffusion into the surrounding tissues. Chen et al. integrated a piezoelectric transducer with a DLP-printed structure consisting of hollow MNs and a tube to facilitate the injection of drugs (Fig. 5S) [126]. Using methylene blue (MB) as a surrogate drug, Chen et al. demonstrated that the ultrasonic MNs were 3 times as efficacious as the hollow MNs without ultrasound in the diffusion of MB through porcine skin in 4 h. MNs have been looked upon as a solution to the poor permeability of drugs with large molecular weight through the skin. However, Chen et al. has shown that MNs coupled with ultrasound enhanced the permeation of a large molecular weight model drug, BSA, by approximately 2.67 times as compared with MNs without ultrasound in 4 h.

More recently, micro-SLA and programmed shaped deformation (4D printing) have been employed in the fabrication of bioinspired MN arrays with backward-facing curved barbs to improve tissue adhesion (Fig. 5T) [82]. Tissue adhesion and pull-out force of the MN arrays with barbs were significantly stronger than the barbless counterparts (Fig. 5U). Drug release efficiency of the barbed MNs loaded with Rhodamine B was observed to be approximately 2.5 μg in 6 h in a chicken breast skin-barrier model (Fig. 5V).

3.2. Extraction of biological specimen

As skin is the largest organ of the body and is abundant in systemic and local tissue biomarkers [135], MNs have been investigated for their usage in extraction of biofluids such as blood, ISF and tissue samples for disease diagnosis and monitoring [136,137]. Although 70% of our dermis consists of ISF by volume, there has been a lack of efficient and effective way to collect sufficient ISF for analysis with minimal damage to the skin. Current practices for extraction of ISF include suction blisters [138,139] which may be contaminated with intracellular materials and inflammatory markers due to separation of the epidermis from the dermis to create the blister [140], reverse iontophoresis [141] which involves electric current, microdialysis [142] and open flow micro-perfusion [143], both of which involve implanting a semi-permeable membrane or a steel mesh tubing respectively. In contrast, MN offers a relatively fast, minimally-invasive and patient-friendly option in the extraction of human interstitial biofluids, tissues and cells. This has led

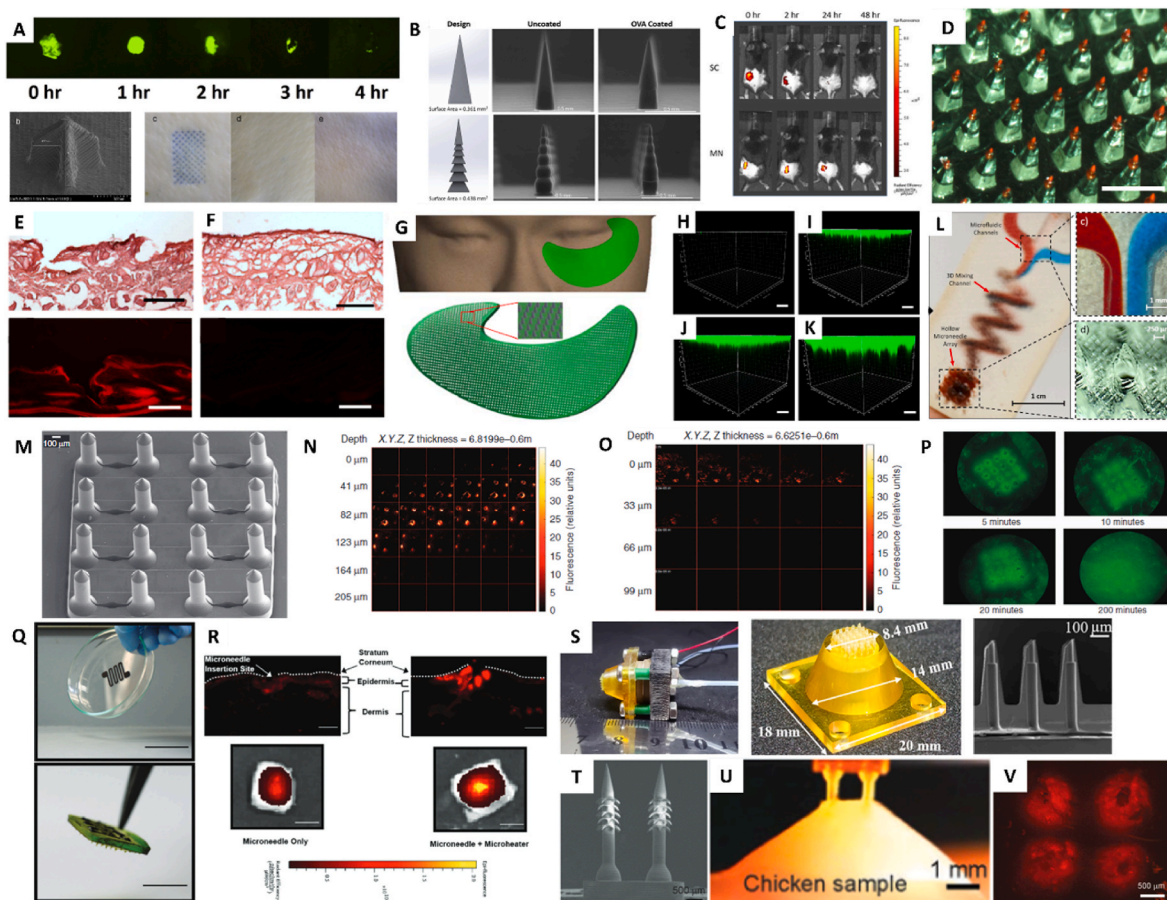


Fig. 5. 3D-printed MNs for transdermal drug delivery. (A) (Top) Fluorescence images of porcine skin over 4h after coated-MN application; (Bottom) SEM image of cross-shaped SLA-printed MN, and porcine skin at various timepoints after applying MB-coated MNs (Adapted with permission from Ref. [60]). (B) CAD and SEM images of CLIP-printed (Top) square pyramidal MNs, and (Bottom) faceted MNs before and after OVA-coating; (C) IVIS live-animal imaging comparing retention of OVA delivered by subcutaneous injection and coated MNs over time (Adapted with permission from Ref. [61]). (D) CLIP-printed PCL MNs with rhodamine B-loaded PAA tip (Adapted with permission from Ref. [133]); Hematoxylin and eosin stained cryosections and fluorescence images comparing (E) MN-treated and (F) untreated murine skin (Reproduced with permission from Ref. [133]). (G) CAD models of personalized MN patch applied on eye area and magnified image of the MNs; Confocal images showing calcein dye skin permeation after 18h comparing (H) blank, (I) untreated skin and pre-treating with (J) commercial MN and (K) personalized MN patch (Adapted with permission from Ref. [98]). (L) SLA-printed microfluidic hollow MN device exhibiting its internal components (Adapted with permission from Ref. [79]). (M) SEM image of TPP-printed MNs after application; Multiphoton microscopy images comparing fluorescein penetration in rabbit ear by (N) MN and (O) topical application; (P) Confocal images of fluorescein delivery in rabbit ear at various timepoints after MN application (Adapted with permission from Ref. [114]). (Q) Microheaters printed on glass Petri dish and back of MN patch by MJ; (R) Fluorescence images of rat skin sections comparing (Top) drug distribution and (Bottom) initial deposition of drug, between application by MN only and MN with microheater (Adapted with permission from Ref. [134]). (S) DLP-printed hollow MN array assembled with piezoelectric transducer; MN array with dimensions and SEM image showing side view of the MNs (Adapted with permission from Ref. [126]). (T) SEM image of projection micro-SLA-printed MNs with backward-facing barbs; (U) MN adhering to chicken muscle tissue upon pulling; (V) Fluorescence image of chicken breast skin-barrier model at 0.5 h after application with rhodamine B-loaded MNs (Adapted with permission from Ref. [82]).

to significant research efforts to develop MNs with improved sample collection efficacy and effectiveness [144–147].

MNs have been explored for extracting biofluids passively without the assistance of vacuum pumps. Turner et al. fabricated an SLA-printed hollow MN array incorporated with a lateral flow assay for the detection of C-reactive protein and procalcitonin in ISF [148]. The hollow MN was designed in a teardrop-shape with a hollow channel, which was linked to the space for housing the lateral flow assay (Fig. 6A). This device with 15 MNs was surface modified by PEGylation to increase hydrophilicity to aid the flow of ISF through the channels, which were estimated to allow uptake of at least 22.5 μ L of ISF. Experiments using reservoirs showed that MNs with PEGylation were able to complete the lateral flow assay in 5 min, whereas ISF collected with the non-PEGylation MNs were insufficient to complete the lateral flow assay (Fig. 6B). Although this superior uptake of ISF in a short period shows the potential of the 3D-printed MNs in diagnostics, further investigation has to be conducted

to corroborate the efficacy and effectiveness of the device in human skin.

To improve the extraction rate and volume, devices such as vacuum pumps can be incorporated into the MN to facilitate retrieval. In a study conducted by Szeto et al., inner ear fluid collection was facilitated by a TPP-printed hollow MN, which had an ultra-sharp tip perforating the RWM of guinea pigs (Fig. 6C–E) [81]. This hollow MN was designed in a cone-and-cylinder shape, with the opening at the side of the conical tip and hollow channel through the middle of the MN. The base of the MN was fabricated to accommodate a 30 G stainless steel syringe needle, which was then mounted on an UltraMicroPump. In vivo assessment of the TPP-printed MN revealed that it was able to perforate the RWM of guinea pigs and collect 1 μ L of perilymph from the cochlea without causing long-term damage to hearing. This could potentially be translated to collection of perilymph from the human scala tympani, which is advantageous in inner ear diagnostics.

Besides biofluid extraction, MNs have also been investigated for their

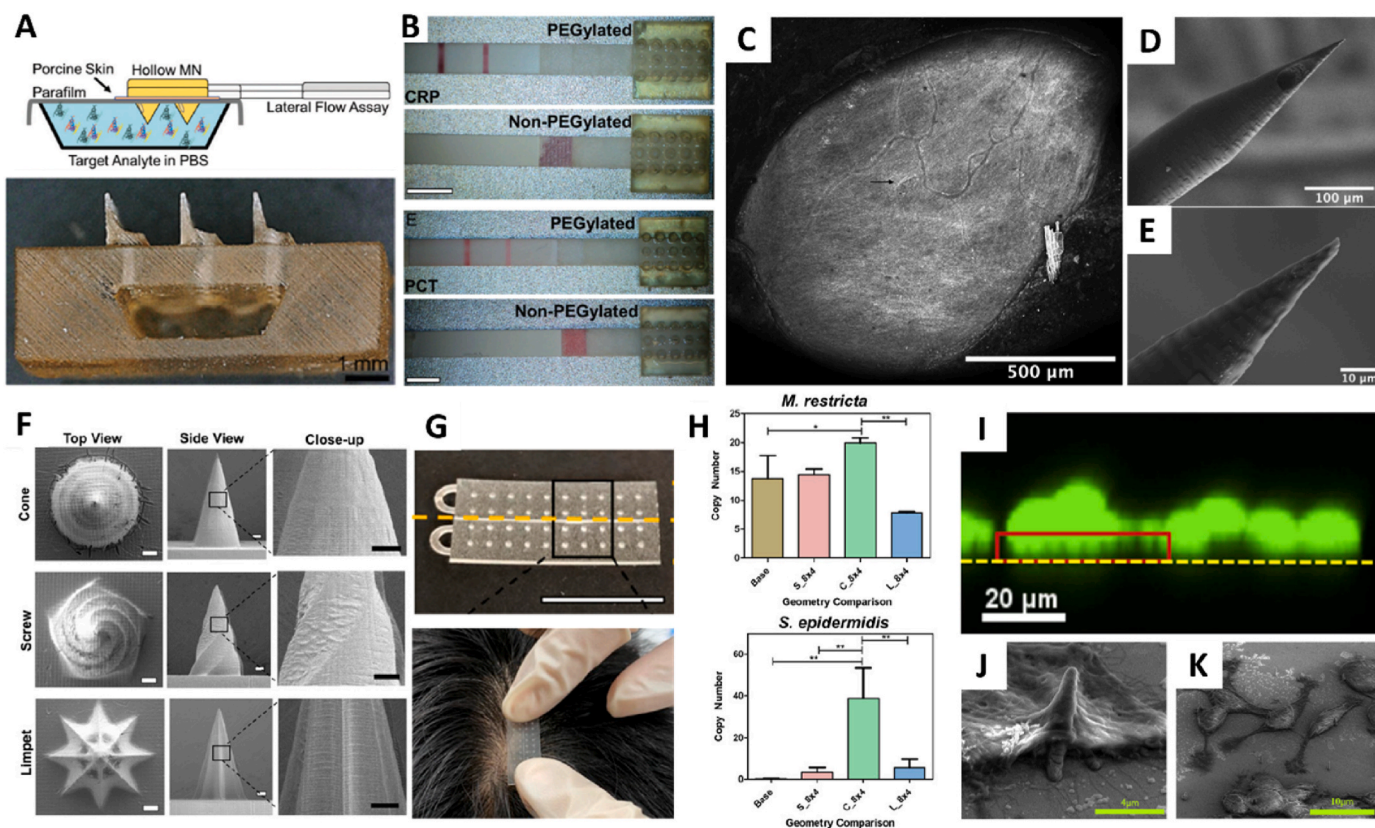


Fig. 6. 3D-printed MNs for extraction of biological specimen. (A) (Top) Schematics showing the mechanism of the lateral flow assay-integrated hollow MN, (Bottom) Optical image showing the SLA-printed hollow MNs and channels linked to a space for housing the lateral flow assay; (B) Images comparing the extraction capabilities of PEGylated and non-PEGylated MNs using (top) C-reactive protein and (bottom) procalcitonin solution (Adapted with permission from Ref. [148]). (C) Confocal image showing location of perforation (black arrow) by the TPP-printed hollow MN in the RWM, 72h after perforation; SEM images with magnification of (D) 134x and (E) 1540X, showing intact TPP-printed hollow MN showing intact TPP-printed hollow MN after using for perforation of RWM (Reproduced with permission from Ref. [81]). (F) SEM images of top and side view of MNs with Cone, Screw and Limpet geometries; (G) (Top) Image showing the collapsible 3D-printed transepidermal MN and (bottom) sampling microbiome from the scalp using the optimized MN patch; (H) Plot comparing efficacies of various MN geometries in picking up (top) *M. restricta* and (bottom) *S. epidermidis* (Adapted with permission from Ref. [149]). (I) Confocal images of calcein AM-stained cells wrapping around MNs (black protrusions bounded by a red rectangle); SEM images showing (J) MN-cell interaction where a cell enfolds itself around a TPP-printed cylindrical MN, and (K) adhesion of cells on the MN array after seeding (Adapted with permission from Ref. [113]).

ability to extract skin microbiome as well as cellular content from single cells. To evaluate the optimal design for skin microbiome extraction, Liang et al. leveraged on the rapid customizability of DLP manufacture to fabricate MNs of various lengths, geometries and needle densities (Fig. 6F) [149]. The optimized MN demonstrated the ability to extract transepidermal microbes from the scalp of human subjects (Fig. 6G), with a higher fungi diversity as compared to conventional collection method such as swab and tape-strip. Kavaldzhiev et al. demonstrated the potential of using biocompatible MNs to retrieve cellular material after MN internalization (Fig. 6H–J) [113]. MNs were fabricated by TPP on a silicon substrate with a needle height of $6\ \mu\text{m}$ and diameter of $630 \pm 15\ \text{nm}$. As the colon cancer cells exhibit a mean diameter of $15.4\ \mu\text{m}$ [150, 151], one MN of that size would be able to penetrate approximately halfway into the cell's body. This can potentially be used for the extraction and analysis of single-cells for diagnostic purposes, as well as enhancement of drug delivery and tissue engineering.

3.3. Biosensing

Electrochemical biosensor is the most common biosensing technique used in MNs, which involves the detection of biological or chemical analytes in the body through physicochemical signals generated during reactions [152,153]. Since MNs are able to bypass the stratum corneum to assess the dermal ISF rich in biomarkers and also transepidermal layers below the epidermis, MN-based biosensors allow for real-time

analysis without the need to extract ISF or diseased tissue for further processing in the clinical laboratories. From the clinical perspective, this process is less cumbersome and enables shorter duration to results. As such, MN biosensors have since been explored in disease diagnostics [154–156], and health monitoring [157,158], to provide a wearable, minimally-invasive option for real-time monitoring of body conditions or rapid detection of diseased tissues.

MN electrodes have been used to detect biomarkers in dermal fluids for health and disease monitoring. Miller et al. designed a K^+ ion selective electrode (ISE) based on MN to monitor K^+ levels for diagnostic purposes (Fig. 7A–C) [155]. The ISE was made from the solid state of porous carbon K^+ ion and incorporated into a microfluidic chip with a TPP-fabricated hollow MN, creating a three-electrode MN system within the microfluidic chip. The ISE was able to detect increasing KCl concentrations and rapidly stabilize potential values. The calibration slope obtained was close to Nernstian value at $57.9\ \text{mV}$ per decade, with activity range from 10^{-5} to $10^{-2}\ \text{M}$ and detection limit of $10^{-5.65}\ \text{M}$ (Fig. 7D), which had comparable capabilities with other carbon-based ISE [159]. This technology can be further developed to detect other biomarkers, thus paving the way for future advancements in MN-facilitated biosensing.

Potential use of MN electrodes for detection of tumour cell biomarkers in the skin have also been investigated, providing a breakthrough in skin cancer detection and diagnostics. Ciui et al., incorporated electrochemical DLP-printed hollow MN sensors within a

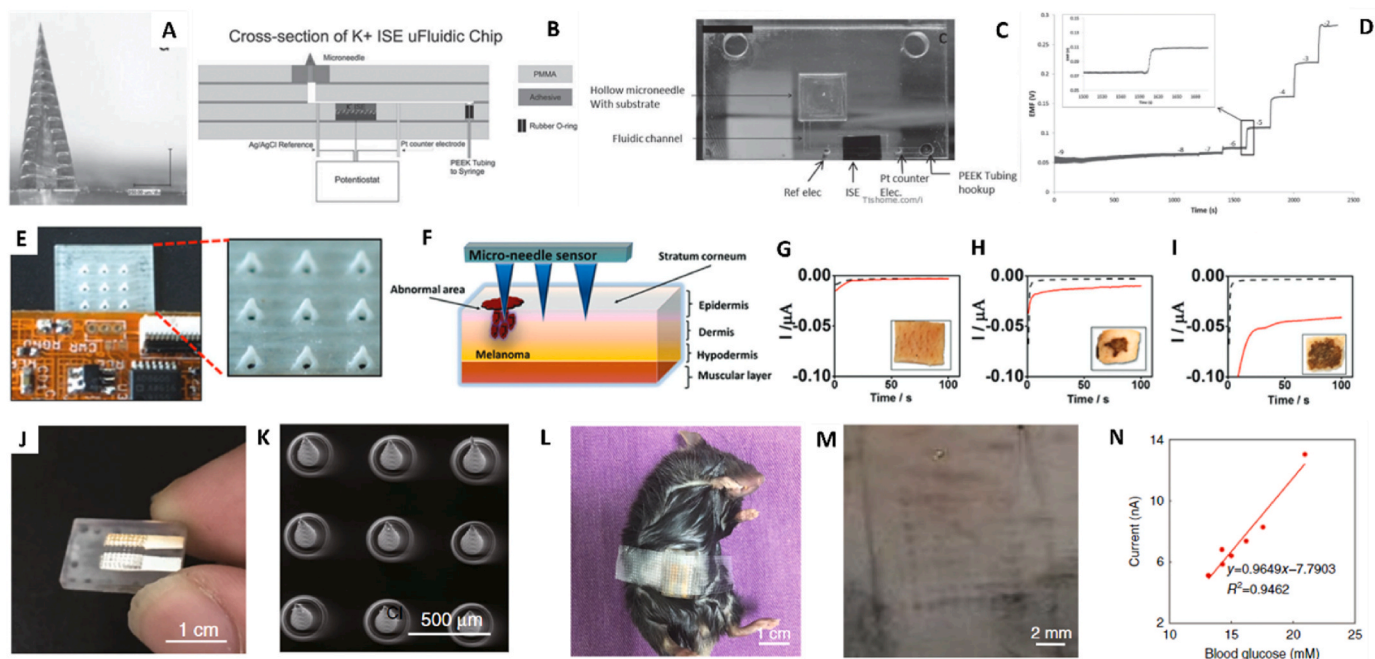


Fig. 7. 3D-printed MNs for biosensing. (A) TPP-printed hollow MN for measuring K⁺ concentrations; (B) Rendering by CorelDraw illustrating the cross-sectional schematics of the ISE microfluidic chip with TPP-printed MN incorporated; (C) Image showing TPP-printed hollow MN incorporated in a microfluidic chip (Adapted with permission from Ref. [155]); (D) Graphs showing EMF measurements in response to increasing concentrations of KCl using a porous carbon K⁺ ISE electrode with a magnified image of the EMF measurements during a KCl concentration spike (Reproduced with permission from Ref. [155]). (E) DLP-printed hollow MNs incorporated with soft flexible electronics; (F) Diagram showing MN sensor inserted in a melanoma for detection of melanoma biomarker; Chronoamperometric plots showing amperometric measurements made by the TPP-printed hollow MN sensor before (black dotted line) and after (red line) insertion into porcine skin treated with (G) 0 mg/mL, (H) 0.5 mg/mL and (I) 2.5 mg/mL TYR (Adapted with permission from Ref. [154]). (J) Electrochemical sensor integrated MN for continuous glucose monitoring; (K) SEM image of conical MNs printed using a high resolution DLP printer; (L) Microneedle biosensor inserted and taped to a mouse for *in vivo* monitoring of subcutaneous glucose. (M) MN pores on mouse abdomen skin after MN biosensor application; (N) Graph showing correlation between subcutaneous glucose and blood glucose levels measured by MN biosensor and a commercial glucose meter respectively, in an insulin-injected diabetic mouse (Adapted with permission from Ref. [160]).

wearable bandage for the detection of melanoma (Fig. 7E–F) [154]. The hollow MNs were filled with catechol-coated carbon paste, which is the substrate of tyrosinase (TYR), an enzyme commonly found in melanoma. The hollow MN sensors were able to differentiate between untreated and porcine skin treated with TYR, while also successfully detecting varying levels of TYR in the skin (Fig. 7G–I). With this device, TYR levels in skin tissues can be assessed, allowing early detection of melanoma which reduces the risk of metastasis and mortality.

Liu et al. fabricated a TPP-printed MN for integrated with electrodes for continuous glucose detection (Fig. 7J–K) [160]. The electrodes were made by firstly evaporating Au and Ag onto the TPP-printed MNs, which was subsequently electroplated with Prussian Blue. *In vivo* assessment in mice revealed that the blood glucose concentrations measured using the integrated MN biosensing device corroborated well with the commercial blood glucose meter, with R^2 of 0.9657 (Fig. 7L–N). This suggests that MNs can provide a potential accurate method for minimally invasive monitoring of blood glucose.

4. Conclusion and future works

This review introduces the 3D printing technologies employed in the fabrication of MNs and critically analyses the benefits and limitations of each approach, and provides an insight into the current and emerging applications for the 3D-printed MNs. The advantages of 3D printing, including its high resolution, high customizability, compatibility with biomaterials, and its one-step fabrication process, have enabled the manufacture of novel complex MNs and improved their efficacies in various biomedical applications.

The appeal of 3D printing for MNs is the easy customizability whilst conveniently involving only a one-step fabrication process. One major

advantage of easy customizability, apart from being able to rapidly create prototypes, is the ability to cater for personalized treatment, similar to how personalized casts [161] or prosthetics [162] are being 3D-printed for patients in hospitals. One difficulty faced in clinical settings for transdermal application of MNs is having to ensure that the MN remains inserted in the skin until the MN is fully dissolved [66], which is not only inconvenient, but could also possibly result in insufficient dosing when MN patches are removed before fully dissolving [67]. Furthermore, micromolding, as the most common method of large-scale fabrication of MNs, adopts a one-size-fits-all methodology and is unable to cater to different skin conditions of patients or the contours of the body surfaces [98,163]; hence, 3D printing would be a better choice in such cases. In particular, 3D-printed MNs may be an appealing choice for cosmeceutical applications, as the size of the MN patch may be easily altered to fit the target areas and conform to the contours of the face, while the height of the MNs can be easily controlled for different areas of the face as certain areas of the facial skin is more delicate as compared with skin in most other parts of the body. In addition, 3D-printed MNs provide the option for varying drug dosing, which may be required for different stages of treatment especially for long-term treatments [164]. Furthermore, the high resolution of 3D printing offers the opportunity for MNs to be used in dimensional accuracy-demanding applications where there is little room for errors in dimensions, such as the ocular [165–167] or vascular tissues [125,168].

Apart from transdermal delivery, 3D-printed MNs can be exploited for delivery of therapeutics non-transdermally to other tissues, organs and sites of injury [169], such as oral mucosa [170], cardiac tissue [77, 171] and wounds [172]. In addition to small molecular drugs, MNs can also be used to deliver biological products, especially macromolecules, thus providing a viable option for vaccinations [173,174] and treatment

of complex diseases that require complicated treatments such as proteins, genes, drugs and metal ions combination therapies [175,176]. Besides delivery, 3D printing fabrication of MNs could be harnessed for skin tissue biopsy or cytology applications. To aid the diagnosis of skin cancers and inflammation, Lin et al. have developed a lancet-like micro biopsy device that captured a small amount of peripheral blood and lysed skin cell materials [177]. With the ability of 3D printing to generate MNs to a specific depth of interest for collection of tissues, MNs can potentially be designed to extract small tissue and cellular samples for clinical analysis, circumventing the use of more invasive biopsy punches. Collectively, in the fields of these highly sensitive areas as precise control and alteration of penetration depth and mechanical properties are required, 3D printing manufacture of MNs will become increasingly attractive.

The global market for MN-based drug delivery systems was forecasted to grow at a Compound Annual Growth Rate (CAGR) of 7.10% in the period of 2020–2027 [178], indicating the increasing demand for commercial MN products. Since the introduction of MN as a potential device in the 1990s, few have obtained the Food and Drug Administration (FDA) clearance to advance into the market. Some of the notable few FDA-approved MN devices include MicronJet™ (Nanopass Technologies Ltd.) for vaccination, Abbott's Libre system and HemoLink (Tasso Inc.) for blood collection, and MTS Roller™ for cosmetic purposes. Fuelled by the burgeoning market for MN delivery systems, we expect greater efforts to catalyze the commercialization of MNs and 3D printing of MNs for niche, personalized applications which may play an important role in accelerating this progress in the near future.

Despite the promises, some key challenges including scalability and regulation which have to be overcome to elevate 3D-printed MNs closer to market. As the adoption of 3D printing in MN fabrication is relatively new, it would take some time to establish large-scale production processes and work streams. From the manufacturer's standpoint, it will be important to consider and evaluate the cost efficiency of 3D printing for mass production in comparison to traditional MN fabrication methods such as micromolding. Owing to the trade-off between print resolution and build size, the advancement of printing technologies may also be critical to enable scalable and consistent production. Concurrently, the institution of defined regulatory pathways for 3D-printed MNs is needed to facilitate entry into market. In terms of MN devices, a final guidance for MN devices under "Regulatory Considerations for Microneedling Products" [179] coupled with Quality systems (QS) regulations under 21 CFR Part 820 [180] have been released by FDA. Similar guidelines can be found in ISO 13485:2016 "Medical devices – Quality management systems – Requirements for regulatory purposes" [181]. On the other hand, there is less clarity on the regulations for 3D-printed medical devices or therapeutics as they have not been thoroughly investigated. Nevertheless, the draft guidance "Technical Considerations for Additive Manufactured Medical Devices" issued by FDA in 2016 for 3D-printed medical devices could offer some insights on some of the factors to consider for regulatory approval [182].

As the implementation of 3D printing technologies in the fabrication of MNs is in the nascent stages, most of the innovations are still at the research or preclinical level. Nevertheless, with the potential of 3D printing to achieve a high level of personalization, customizability, and resolution that is unattainable through conventional methods, it is expected to facilitate the design and manufacture of next generation MNs in therapeutics, diagnostics, as well as cosmeceuticals.

Ethics approval and consent to participate

This study does not perform any experiments on animals or human subjects and did not require local ethics committee approval.

CRediT authorship contribution statement

Jia Min Loh: Conceptualization, Project administration, Writing –

original draft. **Yun Jie Larissa Lim:** Writing – original draft. **Jin Ting Tay:** Writing – original draft. **Hui Mei Cheng:** Resources, Writing – review & editing. **Hong Liang Tey:** Resources, Writing – review & editing. **Kun Liang:** Conceptualization, Funding acquisition, Resources, Supervision, Writing – review & editing.

Declaration of competing interest

The authors declare no conflicts of interest.

Acknowledgments

This work is supported by the National Additive Manufacturing Innovative Cluster (NAMIC) POC Funding, Agency for Science, Technology and Research (A*STAR) Career Development Fund and BMRC Central Research Fund (CRF, ATR) and NHG Medical Technologies & Innovations (CMTi) and National Health Innovation Centre Singapore (NHIC) Joint MedTech Grant.

References

- [1] S. Henry, D.V. McAllister, M.G. Allen, M.R. Prausnitz, Microfabricated microneedles: a novel approach to transdermal drug delivery, *J Pharm Sci* 87 (1998) 922–925, <https://doi.org/10.1021/js980042+>.
- [2] F.M. Hendriks, D. Brokken, C.W.J. Oomens, D.L. Bader, F.P.T. Baaijens, The relative contributions of different skin layers to the mechanical behavior of human skin in vivo using suction experiments, *Med. Eng. Phys.* 28 (2006) 259–266, <https://doi.org/10.1016/j.medengphy.2005.07.001>.
- [3] M. Schneider, F. Stracke, S. Hansen, U.F. Schaefer, Nanoparticles and their interactions with the dermal barrier, *Dermatoendocrinol* 1 (2009) 197–206, <https://doi.org/10.4161/derm.1.4.9501>.
- [4] H.I. Labouta, M. Schneider, Interaction of inorganic nanoparticles with the skin barrier: current status and critical review, *Nanomedicine* 9 (2013) 39–54, <https://doi.org/10.1016/j.nano.2012.04.004>.
- [5] Y. Hao, W. Li, X.L. Zhou, F. Yang, Z.Y. Qian, Microneedles-based transdermal drug delivery systems: a review, *J. Biomed. Nanotechnol.* 13 (2017) 1581–1597, <https://doi.org/10.1166/jbn.2017.2474>.
- [6] X. Li, W. Shan, Y. Yang, D. Joramoon, Y. Zhu, Y. Chen, Y. Yuan, H. Xu, J. Kong, R. Dai, Q. Nian, Y. Chai, Y. Chen, Limpet tooth-inspired painless microneedles fabricated by magnetic field-assisted 3D printing, *Adv. Funct. Mater.* 31 (2021) 1–11, <https://doi.org/10.1002/adfm.202003725>.
- [7] S. Bhatnagar, K. Dave, V.V.K. Venuganti, Microneedles in the clinic, *J. Contr. Release* 260 (2017) 164–182, <https://doi.org/10.1016/j.jconrel.2017.05.029>.
- [8] M.A. Luzuriaga, D.R. Berry, J.C. Reagan, R.A. Smaldone, J.J. Gassensmith, Biodegradable 3D printed polymer microneedles for transdermal drug delivery, *Lab Chip* 18 (2018) 1223–1230, <https://doi.org/10.1039/c8lc00098k>.
- [9] J.D. Bos, M.M.H.M. Meinardi, The 500 Dalton rule for the skin penetration of chemical compounds and drugs, *Exp. Dermatol.* 9 (2000) 165–169, <https://doi.org/10.1034/j.1600-0625.2000.009003165.x>.
- [10] H. Du, P. Liu, J. Zhu, J. Lan, Y. Li, L. Zhang, J. Zhu, J. Tao, Hyaluronic acid-based dissolving microneedle patch loaded with methotrexate for improved treatment of psoriasis, *ACS Appl. Mater. Interfaces* 11 (2019) 43588–43598, <https://doi.org/10.1021/acsami.9b15668>.
- [11] Y. Kim, S.A. Bhattacharjee, M. Beck-Broichsitter, A.K. Banga, Fabrication and characterization of hyaluronic acid microneedles to enhance delivery of magnesium ascorbyl phosphate into skin, *Biomed. Microdevices* 21 (2019) 104, <https://doi.org/10.1007/s10544-019-0455-0>.
- [12] Y. Hao, Y. Chen, M. Lei, T. Zhang, Y. Cao, J. Peng, L. Chen, Z. Qian, Near-infrared responsive PEGylated gold nanorod and doxorubicin loaded dissolvable hyaluronic acid microneedles for human epidermal cancer therapy, *Adv. Ther.* 1 (2018), 1800008, <https://doi.org/10.1002/adtp.201800008>.
- [13] Y. Xie, H. Wang, J. Mao, Y. Li, M. Hussain, J. Zhu, Y. Li, L. Zhang, J. Tao, J. Zhu, Enhanced in vitro efficacy for inhibiting hypertrophic scar by bleomycin-loaded dissolving hyaluronic acid microneedles, *J. Mater. Chem. B* 7 (2019) 6604–6611, <https://doi.org/10.1039/C9TB01449G>.
- [14] D. Wu, X. Shou, Y. Yu, X. Wang, G. Chen, Y. Zhao, L. Sun, Biologics-loaded photothermally dissolvable hyaluronic acid microneedle patch for psoriasis treatment, *Adv. Funct. Mater.* 32 (2022), 2205847, <https://doi.org/10.1002/adfm.202205847>.
- [15] Y.Y. Chun, W.W.R. Tan, M.I.G. Vos, W.K. Chan, H.L. Tey, N.S. Tan, T.T.Y. Tan, Scar prevention through topical delivery of gelatin-tyramine-siSPARC nanoplex loaded in dissolvable hyaluronic acid microneedle patch across skin barrier, *Biomater. Sci.* 10 (2022) 3963–3971, <https://doi.org/10.1039/D2BM00572G>.
- [16] A. Than, K. Liang, S. Xu, L. Sun, H. Duan, F. Xi, C. Xu, P. Chen, Transdermal delivery of anti-obesity compounds to subcutaneous adipose tissue with polymeric microneedle patches, *Small Methods* 1 (2017), 1700269, <https://doi.org/10.1002/smt.201700269>.
- [17] H. Du, P. Liu, J. Zhu, J. Lan, Y. Li, L. Zhang, J. Zhu, J. Tao, Hyaluronic acid-based dissolving microneedle patch loaded with methotrexate for improved treatment

- of psoriasis, *ACS Appl. Mater. Interfaces* 11 (2019) 43588–43598, <https://doi.org/10.1021/acsami.9b15668>.
- [18] H.X. Nguyen, B.D. Bozorg, Y. Kim, A. Wieber, G. Birk, D. Lubda, A.K. Banga, Poly (vinyl alcohol) microneedles: fabrication, characterization, and application for transdermal drug delivery of doxorubicin, *Eur. J. Pharm. Biopharm.* 129 (2018) 88–103, <https://doi.org/10.1016/j.ejpb.2018.05.017>.
- [19] X.P. Zhang, B.B. Wang, W.X. Li, W.M. Fei, Y. Cui, X.D. Guo, In vivo safety assessment, biodistribution and toxicology of polyvinyl alcohol microneedles with 160-day uninterrupted applications in mice, *Eur. J. Pharm. Biopharm.* 160 (2021) 1–8, <https://doi.org/10.1016/j.ejpb.2021.01.005>.
- [20] W. Sun, Z. Araci, M. Inayathullah, S. Manickam, X. Zhang, M.A. Bruce, M. P. Marinkovich, A.T. Lane, C. Milla, J. Rajadas, M.J. Butte, Polyvinylpyrrolidone microneedles enable delivery of intact proteins for diagnostic and therapeutic applications, *Acta Biomater.* 9 (2013) 7767–7774, <https://doi.org/10.1016/j.actbio.2013.04.045>.
- [21] D. Liu, B. Yu, G. Jiang, W. Yu, Y. Zhang, B. Xu, Fabrication of composite microneedles integrated with insulin-loaded CaCO₃ microparticles and PVP for transdermal delivery in diabetic rats, *Mater. Sci. Eng. C* 90 (2018) 180–188, <https://doi.org/10.1016/j.msec.2018.04.055>.
- [22] S.P. Sullivan, N. Murthy, M.R. Prausnitz, Minimally invasive protein delivery with rapidly dissolving polymer microneedles, *Adv. Mater.* 20 (2008) 933–938, <https://doi.org/10.1002/adma.200701205>.
- [23] Y. Park, J. Park, G.S. Chu, K.S. Kim, J.H. Sung, B. Kim, Transdermal delivery of cosmetic ingredients using dissolving polymer microneedle arrays, *Biotechnol. Bioproc. Eng.* 20 (2015) 543–549, <https://doi.org/10.1007/s12257-014-0775-0>.
- [24] S. Rojekar, L.K. Vora, I.A. Tekko, F. Volpe-Zanutto, H.O. McCarthy, P.R. Vavia, R. F. Donnelly, Etravirine-loaded dissolving microneedle arrays for long-acting delivery, *Eur. J. Pharm. Biopharm.* 165 (2021) 41–51, <https://doi.org/10.1016/j.ejpb.2021.04.024>.
- [25] E. Altuntaş, I.A. Tekko, L.K. Vora, N. Kumar, R. Brodsky, O. Chevallier, E. McAlister, Q. Kurnia Anjani, H.O. McCarthy, R.F. Donnelly, Nestorone nanosuspension-loaded dissolving microneedles array patch: a promising novel approach for “on-demand” hormonal female-controlled pericoital contraception, *Int. J. Pharm.* 614 (2022), 121422, <https://doi.org/10.1016/j.ijpharm.2021.121422>.
- [26] Y. Wu, L.K. Vora, R.F. Donnelly, T.R.R. Singh, Rapidly dissolving bilayer microneedles enabling minimally invasive and efficient protein delivery to the posterior segment of the eye, *Drug Deliv. Trans. Res.* (2022), <https://doi.org/10.1007/s13346-022-01190-x>.
- [27] D. Ramadan, F. Ulayya, A.S. Qur'ani, I. Iskandarsyah, Y. Harahap, Q.K. Anjani, V. Aileen, P. Hartrianti, R.F. Donnelly, Combination of dissolving microneedles with nanosuspension and Co-grinding for transdermal delivery of ketoprofen, *Pharmaceuticals* 16 (2023) 378, <https://doi.org/10.3390/ph16030378>.
- [28] J. Zhu, X. Zhou, H. Kim, M. Qu, X. Jiang, K. Lee, L. Ren, Q. Wu, C. Wang, X. Zhu, P. Tebon, S. Zhang, J. Lee, N. Ashammakhi, S. Ahadian, M.R. Dokmeci, Z. Gu, W. Sun, A. Khademhosseini, Gelatin methacryloyl microneedle patches for minimally invasive extraction of skin interstitial fluid, *Small* 16 (2020), 1905910, <https://doi.org/10.1002/smll.201905910>.
- [29] D.F.S. Fonseca, P.C. Costa, I.F. Almeida, P. Dias-Pereira, I. Correia-Sá, V. Bastos, H. Oliveira, C. Vilela, A.J.D. Silvestre, C.S.R. Freire, Swellable gelatin methacryloyl microneedles for extraction of interstitial skin fluid toward minimally invasive monitoring of urea, *Macromol. Biosci.* 20 (2020), 2000195, <https://doi.org/10.1002/mabi.202000195>.
- [30] S. Park, Y.J. Kim, S. Park, H. Hong, J. Lee, S. Il Kim, K. Lee, W. Ryu, Rapid extraction and detection of biomolecules via a microneedle array of wet-crosslinked methacrylated hyaluronic acid, *Adv. Mater. Technol.* 7 (2022), 2100874, <https://doi.org/10.1002/admt.202100874>.
- [31] D.D. Zhu, L.W. Zheng, P.K. Duong, R.H. Cheah, X.Y. Liu, J.R. Wong, W.J. Wang, S. T. Tien Guan, X.T. Zheng, P. Chen, Colorimetric microneedle patches for multiplexed transdermal detection of metabolites, *Biosens. Bioelectron.* 212 (2022), 114412, <https://doi.org/10.1016/j.bios.2022.114412>.
- [32] S.W.T. Chew, A.H. Shah, M. Zheng, H. Chang, C. Wiraja, T.W.J. Steele, C. Xu, A self-adhesive microneedle patch with drug loading capability through swelling effect, *Bioeng Transl. Med.* 5 (2020), <https://doi.org/10.1002/btm2.10157>.
- [33] K. Qin, Y. Gui, Y. Li, X. Li, F. Meng, D. Han, L. Du, S. Li, Y. Wang, H. Zhou, H. Yan, Y. Peng, Z. Gao, Biodegradable microneedle array-mediated transdermal delivery of dimethylxylglycine-functionalized zeolitic imidazolate framework-8 nanoparticles for bacteria-infected wound treatment, *ACS Appl. Mater. Interfaces* 15 (2023) 6338–6353, <https://doi.org/10.1021/acsami.2c17328>.
- [34] D. Shin, J. Hyun, Silk fibroin microneedles fabricated by digital light processing 3D printing, *J. Ind. Eng. Chem.* 95 (2021) 126–133, <https://doi.org/10.1016/j.jiec.2020.12.011>.
- [35] S. Wang, M. Zhu, L. Zhao, D. Kuang, S.C. Kundu, S. Lu, Insulin-loaded silk fibroin microneedles as sustained release system, *ACS Biomater. Sci. Eng.* 5 (2019) 1887–1894, <https://doi.org/10.1021/acsbiomaterials.9b00229>.
- [36] Z. Yin, D. Kuang, S. Wang, Z. Zheng, V.K. Yadavalli, S. Lu, Swellable silk fibroin microneedles for transdermal drug delivery, *Int. J. Biol. Macromol.* 106 (2018) 48–56, <https://doi.org/10.1016/j.ijbiomac.2017.07.178>.
- [37] J.W. Lee, J.H. Park, M.R. Prausnitz, Dissolving microneedles for transdermal drug delivery, *Biomaterials* 29 (2008) 2113–2124, <https://doi.org/10.1016/j.biomaterials.2007.12.048>.
- [38] M. Wang, L. Hu, C. Xu, Recent advances in the design of polymeric microneedles for transdermal drug delivery and biosensing, *Lab Chip* 17 (2017) 1373–1387, <https://doi.org/10.1039/C7LC00016B>.
- [39] M.R. Prausnitz, Engineering microneedle patches for vaccination and drug delivery to skin, *Annu. Rev. Chem. Biomol. Eng.* 8 (2017) 177–200, <https://doi.org/10.1146/annurev-chembioeng-060816-101514>.
- [40] A.M.M. Römgen, D.L.L. Bader, J.A.A. Bouwstra, F.P.T.P.T. Baaijens, C.W.J.W. J. Oomens, Monitoring the penetration process of single microneedles with varying tip diameters, *J. Mech. Behav. Biomed. Mater.* 40 (2014) 397–405, <https://doi.org/10.1016/j.jmbmm.2014.09.015>.
- [41] K.J. Krieger, N. Bertollo, M. Dangol, J.T. Sheridan, M.M. Lowery, E. D. O’Cearbhaill, Simple and customizable method for fabrication of high-aspect ratio microneedle molds using low-cost 3D printing, *Microsyst. Nanoeng.* 5 (2019), <https://doi.org/10.1038/s41378-019-0088-8>.
- [42] J.-H. Park, M.G. Allen, M.R. Prausnitz, Biodegradable polymer microneedles: fabrication, mechanics and transdermal drug delivery, *J. Contr. Release* 104 (2005) 51–66, <https://doi.org/10.1016/j.jconrel.2005.02.002>.
- [43] M.C. Chen, M.H. Ling, K.Y. Lai, E. Pramudityo, Chitosan microneedle patches for sustained transdermal delivery of macromolecules, *Biomacromolecules* 13 (2012) 4022–4031, <https://doi.org/10.1021/bm301293d>.
- [44] F.J. Verbaan, S.M. Bal, D.J. van den Berg, W.H.H. Groenink, H. Verpoorten, R. Lüttge, J.A. Bouwstra, Assembled microneedle arrays enhance the transport of compounds varying over a large range of molecular weight across human dermatomed skin, *J. Contr. Release* 117 (2007) 238–245, <https://doi.org/10.1016/j.jconrel.2006.11.009>.
- [45] T. Watanabe, K. Hagino, T. Sato, Evaluation of the effect of polymeric microneedle arrays of varying geometries in combination with a high-velocity applicator on skin permeability and irritation, *Biomed. Microdevices* 16 (2014) 591–597, <https://doi.org/10.1007/s10544-014-9861-5>.
- [46] A. Ripolin, J. Quinn, E. Larrañeta, E.M. Vicente-Perez, J. Barry, R.F. Donnelly, Successful application of large microneedle patches by human volunteers, *Int. J. Pharm.* 521 (2017) 92–101, <https://doi.org/10.1016/j.ijpharm.2017.02.011>.
- [47] H.S. Gill, D.D. Denson, B.A. Burris, M.R. Prausnitz, Effect of microneedle design on pain in human volunteers, *Clin. J. Pain* 24 (2008) 585–594, <https://doi.org/10.1097/AJP.0b013e31816778f9>.
- [48] R.F. Donnelly, M.J. Garland, D.I.J. Morrow, K. Migalska, T.R.R. Singh, R. Majithiya, A.D. Woolfson, Optical coherence tomography is a valuable tool in the study of the effects of microneedle geometry on skin penetration characteristics and in-skin dissolution, *J. Contr. Release* 147 (2010) 333–341, <https://doi.org/10.1016/j.jconrel.2010.08.008>.
- [49] S.M. Bal, J. Caussin, S. Pavel, J.A. Bouwstra, In vivo assessment of safety of microneedle arrays in human skin, *Eur. J. Pharmaceut. Sci.* 35 (2008) 193–202, <https://doi.org/10.1016/j.ejps.2008.06.016>.
- [50] G. Yan, K.S. Warner, J. Zhang, S. Sharma, B.K. Gale, Evaluation needle length and density of microneedle arrays in the pretreatment of skin for transdermal drug delivery, *Int. J. Pharm.* 391 (2010) 7–12, <https://doi.org/10.1016/j.ijpharm.2010.02.007>.
- [51] S.H. Lim, H. Kathuria, M.H. Bin Amir, X. Zhang, H.T.T. Duong, P.C.L. Ho, L. Kang, High resolution photopolymer for 3D printing of personalised microneedle for transdermal delivery of anti-wrinkle small peptide, *J. Contr. Release* 329 (2021) 907–918, <https://doi.org/10.1016/j.jconrel.2020.10.021>.
- [52] M.S. Lhernould, Optimizing hollow microneedles arrays aimed at transdermal drug delivery, *Microsyst. Technol.* 19 (2013) 1–8, <https://doi.org/10.1007/s00542-012-1663-1>.
- [53] I. Xenikakis, M. Tzimtzimis, K. Tsongas, D. Andreadis, E. Demiri, D. Tzetzis, D. G. Fatourous, Fabrication and finite element analysis of stereolithographic 3D printed microneedles for transdermal delivery of model dyes across human skin in vitro, *Eur. J. Pharmaceut. Sci.* 137 (2019), 104976, <https://doi.org/10.1016/j.ejps.2019.104976>.
- [54] R. He, Y. Niu, Z. Li, A. Li, H. Yang, F. Xu, F. Li, A hydrogel microneedle patch for point-of-care testing based on skin interstitial fluid, *Adv. Healthcare Mater.* 9 (2020) 1–11, <https://doi.org/10.1002/adhm.201901201>.
- [55] N. El-Sayed, L. Vaut, M. Schneider, Customized fast-separable microneedles prepared with the aid of 3D printing for nanoparticle delivery, *Eur. J. Pharm. Biopharm.* 154 (2020) 166–174, <https://doi.org/10.1016/j.ejpb.2020.07.005>.
- [56] P. Khanna, H. Silva, S. Bhansali, Variation in microneedle geometry to increase shear strength, *Procedia Eng.* 5 (2010) 977–980, <https://doi.org/10.1016/j.proeng.2010.09.272>.
- [57] W.K. Raja, S. MacCorkle, I.M. Diwan, A. Abdurrob, J. Lu, F.G. Omenetto, D. L. Kaplan, Transdermal delivery devices: fabrication, mechanics and drug release from silk, *Small* 9 (2013) 3704–3713, <https://doi.org/10.1002/smll.201202075>.
- [58] J.-H. Park, M.G. Allen, M.R. Prausnitz, Polymer microneedles for controlled-release drug delivery, *Pharm. Res. (N. Y.)* 23 (2006) 1008–1019, <https://doi.org/10.1007/s11095-006-0028-9>.
- [59] B.P. Chaudhri, F. Ceyssens, T. Guan, A. La Manna, H.P. Neves, C. Van Hoof, R. Puers, High strength, polymer microneedles for transdermal drug delivery, *Procedia Eng.* 25 (2011) 1377–1380, <https://doi.org/10.1016/j.proeng.2011.12.340>.
- [60] M.J. Uddin, N. Scoutaris, S.N. Economidou, C. Giraud, B.Z. Chowdhry, R. F. Donnelly, D. Douroumis, 3D printed microneedles for anticancer therapy of skin tumours, *Mater. Sci. Eng. C* 107 (2020), 110248, <https://doi.org/10.1016/j.msec.2019.110248>.
- [61] C. Caudhill, J.L. Perry, K. Iliadis, A.T. Tessema, B.J. Lee, B.S. Mecham, S. Tian, J. M. DeSimone, Transdermal vaccination via 3D-printed microneedles induces potent humoral and cellular immunity, *Proc. Natl. Acad. Sci. USA* 118 (2021), e2102595118, <https://doi.org/10.1073/pnas.2102595118>.
- [62] W.-G. Bae, H. Ko, J.-Y. So, H. Yi, C.-H. Lee, D.-H. Lee, Y. Ahn, S.-H. Lee, K. Lee, J. Jun, H.-H. Kim, N.L. Jeon, W. Jung, C.-S. Song, T. Kim, Y.-C. Kim, H.E. Jeong, Snake fang-inspired stamping patch for transdermal delivery of liquid

- formulations, *Sci. Transl. Med.* 11 (2019), <https://doi.org/10.1126/scitranslmed.aaw3329>.
- [63] J. Lim, D. Tahk, J. Yu, D.-H. Min, N.L. Jeon, Design rules for a tunable merged-tip microneedle, *Microsyst Nanoeng* 4 (2018) 29, <https://doi.org/10.1038/s41378-018-0028-z>.
- [64] B.M. Torrisi, V. Zarnitsyn, M.R. Prausnitz, A. Anstey, C. Gateley, J.C. Birchall, S. A. Coulman, Pocketed microneedles for rapid delivery of a liquid-state botulinum toxin A formulation into human skin, *J. Contr. Release* 165 (2013) 146–152, <https://doi.org/10.1016/j.jconrel.2012.11.010>.
- [65] Z. Sartawi, C. Blackshields, W. Faisal, Dissolving microneedles: applications and growing therapeutic potential, *J. Contr. Release* 348 (2022) 186–205, <https://doi.org/10.1016/j.jconrel.2022.05.045>.
- [66] P. Xue, X. Zhang, Y.J. Chuah, Y. Wu, Y. Kang, Flexible PEGDA-based microneedle patches with detachable PVP-CD arrowheads for transdermal drug delivery, *RSC Adv.* 5 (2015) 75204–75209, <https://doi.org/10.1039/c5ra09329e>.
- [67] Y. Yang, H. Chu, Y. Zhang, L. Xu, R. Luo, H. Zheng, T. Yin, Z. Li, Rapidly separable bubble microneedle patch for effective local anesthesia, *Nano Res.* 15 (2022) 8336–8344, <https://doi.org/10.1007/s12274-022-4508-y>.
- [68] Z. Chen, Y. Lin, W. Lee, L. Ren, B. Liu, L. Liang, Z. Wang, L. Jiang, Additive manufacturing of honeybee-inspired microneedle for easy skin insertion and difficult removal, *ACS Appl. Mater. Interfaces* 10 (2018) 29338–29346, <https://doi.org/10.1021/acsami.8b09563>.
- [69] M. Guo, Y. Wang, B. Gao, B. He, Shark tooth-inspired microneedle dressing for intelligent wound management, *ACS Nano* 15 (2021) 15316–15327, <https://doi.org/10.1021/acsnano.1c06279>.
- [70] M. Avcil, G. Akman, J. Klokkeers, D. Jeong, A. Çelik, Efficacy of bioactive peptides loaded on hyaluronic acid microneedle patches: a monocentric clinical study, *J. Cosmet. Dermatol.* 19 (2020) 328–337, <https://doi.org/10.1111/jocd.13009>.
- [71] C.-H. Chen, V. Shyu, C.-T. Chen, Dissolving microneedle patches for transdermal insulin delivery in diabetic mice: potential for clinical applications, *Materials* 11 (2018) 1625, <https://doi.org/10.3390/ma11091625>.
- [72] M. Egawa, T. Hirao, M. Takahashi, In vivo estimation of stratum corneum thickness from water concentration profiles obtained with Raman spectroscopy, *Acta Derm. Venereol.* 87 (2007) 4–8, <https://doi.org/10.2340/00015555-0183>.
- [73] J. Sandby-Møller, T. Poulsen, H.C. Wulff, Epidermal thickness at different body sites: relationship to age, gender, pigmentation, blood content, skin type and smoking habits, *Acta Derm. Venereol.* 83 (2003) 410–413, <https://doi.org/10.1080/00015550310015419>.
- [74] T. Liu, G. Luo, M. Xing, Biomedical applications of polymeric microneedles for transdermal therapeutic delivery and diagnosis: current status and future perspectives, *Adv. Ther.* 3 (2020), 1900140, <https://doi.org/10.1002/adtp.201900140>.
- [75] L. Barnum, M. Samandari, T.A. Schmidt, A. Tamayol, Microneedle arrays for the treatment of chronic wounds, *Expert Opin. Drug Deliv.* 17 (2020) 1767–1780, <https://doi.org/10.1080/17425247.2020.1819787>.
- [76] M. Camović, A. Bišević, I. Brčić, K. Borčak, S. Bušatlić, N. Čenanović, A. Dedović, A. Mulalić, M. Osmanlić, M. Širubalo, A. Tucak, E. Vranić, Coated 3D printed PLA microneedles as transdermal drug delivery systems, *IFMBE Proces.* 73 (2020) 735–742, https://doi.org/10.1007/978-3-030-17971-7_109.
- [77] J. Tang, J. Wang, K. Huang, Y. Ye, T. Su, L. Qiao, M.T. Hensley, T.G. Caranasos, J. Zhang, Z. Gu, K. Cheng, Cardiac cell-integrated microneedle patch for treating myocardial infarction, *Sci. Adv.* 4 (2018) 1–13, <https://doi.org/10.1126/sciadv.aat9365>.
- [78] N. Shahrubudin, T.C. Lee, R. Ramlan, An overview on 3D printing technology: technological, materials, and applications, *Procedia Manuf.* 35 (2019) 1286–1296, <https://doi.org/10.1016/j.promfg.2019.06.089>.
- [79] C. Yeung, S. Chen, B. King, H. Lin, K. King, F. Akhtar, G. Diaz, B. Wang, J. Zhu, W. Sun, A. Khademhosseini, S. Emaminejad, A 3D-printed microfluidic-enabled hollow microneedle architecture for transdermal drug delivery, *Biomicrofluidics* 13 (2019), 064125, <https://doi.org/10.1063/1.5127778>.
- [80] K. Moussi, A. Bukhamsin, T. Hidalgo, J. Kosel, Biocompatible 3D printed microneedles for transdermal, intradermal, and percutaneous applications, *Adv. Eng. Mater.* 22 (2020) 1–10, <https://doi.org/10.1002/adem.201901358>.
- [81] B. Szeto, A. Aksit, C. Valentini, M. Yu, E.G. Werth, S. Goeta, C. Tang, L.M. Brown, E.S. Olson, J.W. Kysar, A.K. Lalwani, Novel 3D-printed hollow microneedles facilitate safe, reliable, and informative sampling of perilymph from Guinea pigs, *Hear. Res.* 400 (2021), <https://doi.org/10.1016/j.heares.2020.108141>.
- [82] D. Han, R.S. Morde, S. Mariani, A.A. La Mattina, E. Vignali, C. Yang, G. Barillaro, H. Lee, 4D printing of a bioinspired microneedle array with backward-facing barbs for enhanced tissue adhesion, *Adv. Funct. Mater.* 30 (2020), <https://doi.org/10.1002/adfm.201909197>.
- [83] D. Ghanbariamin, M. Samandari, P. Ghelich, S. Shahbazmohamadi, T.A. Schmidt, Y. Chen, A. Tamayol, Cleanroom-free fabrication of microneedles for multimodal drug delivery, *Small* (2023), <https://doi.org/10.1002/sml.202207131>.
- [84] L. Wu, J. Park, Y. Kamaki, B. Kim, Optimization of the fused deposition modeling-based fabrication process for polylactic acid microneedles, *Microsyst Nanoeng* 7 (2021), <https://doi.org/10.1038/s41378-021-00284-9>.
- [85] O. Diegel, A. Nordin, D. Motte, Additive Manufacturing Technologies, 2019, https://doi.org/10.1007/978-981-13-8281-9_2.
- [86] K. Liang, D. Brambilla, J.-C. Leroux, Is 3D printing of pharmaceuticals a disruptor or enabler? *Adv. Mater.* 31 (2019), 1805680 <https://doi.org/10.1002/adma.201805680>.
- [87] J.H. Lee, J.M. Baik, Y.S. Yu, J.H. Kim, C.B. Ahn, K.H. Son, J.H. Kim, E.S. Choi, J. W. Lee, Development of a heat labile antibiotic eluting 3D printed scaffold for the treatment of osteomyelitis, *Sci. Rep.* 10 (2020) 1–8, <https://doi.org/10.1038/s41598-020-64573-5>.
- [88] A. Chalgham, A. Ehrmann, I. Wickenkamp, Mechanical properties of FDM printed PLA parts before and after thermal treatment, *Polymers* 13 (2021) 1239, <https://doi.org/10.3390/polym13081239>.
- [89] J. Babilotte, B. Martin, V. Guduric, R. Baille, R. Agniel, S. Roques, V. Héroguez, M. Dussauze, M. Gaudon, D. Le Nihouannen, S. Catros, Development and characterization of a PLGA-HA composite material to fabricate 3D-printed scaffolds for bone tissue engineering, *Mater. Sci. Eng. C* 118 (2021), 111334, <https://doi.org/10.1016/j.msec.2020.111334>.
- [90] J. Goole, K. Amighi, 3D printing in pharmaceuticals: a new tool for designing customized drug delivery systems, *Int. J. Pharm.* 499 (2016) 376–394, <https://doi.org/10.1016/j.ijpharm.2015.12.071>.
- [91] E.A. Allen, C. O'Mahony, M. Cronin, T. O'Mahony, A.C. Moore, A.M. Crean, Dissolvable microneedle fabrication using piezoelectric dispensing technology, *Int. J. Pharm.* 500 (2016) 1–10, <https://doi.org/10.1016/j.ijpharm.2015.12.052>.
- [92] S.N. Economidou, C.P.P. Pere, A. Reid, MdJ. Uddin, J.F.C. Windmill, D. A. Lamprou, D. Douroumis, 3D printed microneedle patches using stereolithography (SLA) for intradermal insulin delivery, *Mater. Sci. Eng. C* 102 (2019) 743–755, <https://doi.org/10.1016/j.msec.2019.04.063>.
- [93] C.P.P. Pere, S.N. Economidou, G. Lall, C. Ziraud, J.S. Boateng, B.D. Alexander, D. A. Lamprou, D. Douroumis, 3D printed microneedles for insulin skin delivery, *Int. J. Pharm.* 544 (2018) 425–432, <https://doi.org/10.1016/j.ijpharm.2018.03.031>.
- [94] M.J. Uddin, N. Scoutaris, P. Klepetsanis, B. Chowdhry, M.R. Prausnitz, D. Douroumis, Inkjet printing of transdermal microneedles for the delivery of anticancer agents, *Int. J. Pharm.* 494 (2015) 593–602, <https://doi.org/10.1016/j.ijpharm.2015.01.038>.
- [95] H. Derakhshandeh, F. Aghabaglou, A. McCarthy, A. Mostafavi, C. Wiseman, Z. Bonick, I. Ghanavati, S. Harris, C. Kreikemeier-Bower, S.M. Moosavi Basri, J. Ronseboom, R. Yang, P. Mostafalu, D. Orgill, A. Tamayol, A wirelessly controlled smart bandage with 3D-printed miniaturized needle arrays, *Adv. Funct. Mater.* 30 (2020), 1905544, <https://doi.org/10.1002/adfm.201905544>.
- [96] L. Barnum, J. Quint, H. Derakhshandeh, M. Samandari, F. Aghabaglou, A. Farzin, L. Abbasi, S. Bencherif, A. Memic, P. Mostafalu, A. Tamayol, 3D-Printed hydrogel-filled microneedle arrays, *Adv. Healthcare Mater.* 10 (2021), 2001922, <https://doi.org/10.1002/adhm.202001922>.
- [97] X. Zhang, Y. Xu, L. Li, B. Yan, J. Bao, A. Zhang, Acrylate-based photosensitive resin for stereolithographic three-dimensional printing, *J. Appl. Polym. Sci.* 136 (2019) 1–10, <https://doi.org/10.1002/app.47487>.
- [98] S.H. Lim, W.J. Tiew, J. Zhang, P.C.L. Ho, N.N. Kachouie, L. Kang, Geometrical optimisation of a personalised microneedle eye patch for transdermal delivery of anti-wrinkle small peptide, *Biofabrication* 12 (2020), 35003, <https://doi.org/10.1088/1758-5090/ab6d37>.
- [99] S.N. Economidou, C.P. Pissinato Pere, M. Okereke, D. Douroumis, Optimisation of design and manufacturing parameters of 3d printed solid microneedles for improved strength, sharpness, and drug delivery, *Micromachines* 12 (2021) 1–16, <https://doi.org/10.3390/mi12020117>.
- [100] S. Choo, S. Jin, J. Jung, Fabricating high-resolution and high-dimensional microneedle mold through the resolution improvement of stereolithography 3D printing, *Pharmaceutics* 14 (2022) 766, <https://doi.org/10.3390/pharmaceutics14040766>.
- [101] Z. Wang, R. Fu, X. Han, D. Wen, Y. Wu, S. Li, Z. Gu, Shrinking fabrication of a glucose-responsive glucagon microneedle patch, *Adv. Sci.* 9 (2022), <https://doi.org/10.1002/advs.202203274>.
- [102] R. Naohara, K. Narita, T. Ikeda-Fukuzawa, Change in hydrogen bonding structures of a hydrogel with dehydration, *Chem. Phys. Lett.* 670 (2017) 84–88, <https://doi.org/10.1016/j.cplett.2017.01.006>.
- [103] K. Kowsari, B. Zhang, S. Panjwani, Z. Chen, H. Hingorani, S. Akbari, N.X. Fang, Q. Ge, Photopolymer formulation to minimize feature size, surface roughness, and stair-stepping in digital light processing-based three-dimensional printing, *Addit. Manuf.* 24 (2018) 627–638, <https://doi.org/10.1016/j.addma.2018.10.037>.
- [104] Y. Pan, X. Zhao, C. Zhou, Y. Chen, Smooth surface fabrication in mask projection based stereolithography, *J. Manuf. Process.* 14 (2012) 460–470, <https://doi.org/10.1016/j.jmapro.2012.09.003>.
- [105] L. Lin, Y. Wang, M. Cai, X. Jiang, Y. Hu, Z. Dong, D. Yin, Y. Liu, S. Yang, Z. Liu, J. Zhuang, Y. Xu, C.F. Guo, L. Chang, Multimicrochannel microneedle microporation platform for enhanced intracellular drug delivery, *Adv. Funct. Mater.* 32 (2022), 2109187, <https://doi.org/10.1002/adfm.202109187>.
- [106] B.P. Partlow, M.B. Applegate, F.G. Omenetto, D.L. Kaplan, Dityrosine cross-linking in designing biomaterials, *ACS Biomater. Sci. Eng.* 2 (2016) 2108–2121, <https://doi.org/10.1021/acsbomaterials.6b00454>.
- [107] G. Choi, H.J. Cha, Recent advances in the development of nature-derived photocrosslinkable biomaterials for 3D printing in tissue engineering, *Biomater. Res.* 23 (2019) 1–7, <https://doi.org/10.1186/s40824-019-0168-8>.
- [108] B.J. Lee, K. Hsiao, G. Lipkowitz, T. Samuelsen, L. Tate, J.M. DeSimone, Characterization of a 30 μm pixel size CLIP-based 3D printer and its enhancement through dynamic printing optimization, *Addit. Manuf.* 55 (2022), 102800, <https://doi.org/10.1016/j.addma.2022.102800>.
- [109] N.U. Rajesh, I. Coates, M.M. Driskill, M.T. Dulay, K. Hsiao, D. Ilyin, G. B. Jacobson, J.W. Kwak, M. Lawrence, J. Perry, C.O. Shea, S. Tian, J. M. Desimone, 3D-Printed microarray patches for transdermal applications, *J. Am. Chem. Soc.* (2022), <https://doi.org/10.1021/jacsau.2c00432>.
- [110] A. Aksit, D.N. Arteaga, M. Arriaga, X. Wang, H. Watanabe, K.E. Kasza, A. K. Lalwani, J.W. Kysar, In-vitro perforation of the round window membrane via direct 3-D printed microneedles, *Biomed. Microdevices* 20 (2018), <https://doi.org/10.1007/s10544-018-0287-3>.
- [111] I. Sakellari, E. Kabouraki, D. Gray, V. Purlis, C. Fotakis, A. Pikulin, N. Bityurin, M. Vamvakaki, M. Farsari, Diffusion-assisted high-resolution direct femtosecond

- laser writing, *ACS Nano* 6 (2012) 2302–2311, <https://doi.org/10.1021/nl204454c>.
- [112] D.K. Limberg, J.-H. Kang, R.C. Hayward, Triplet–triplet annihilation photopolymerization for high-resolution 3D printing, *J. Am. Chem. Soc.* 144 (2022) 5226–5232, <https://doi.org/10.1021/jacs.1c11022>.
- [113] M. Kavaldzhiev, J.E. Perez, Y. Ivanov, A. Bertoncini, C. Liberale, J. Kosel, Biocompatible 3D printed magnetic micro needles, *Biomed Phys. Eng. Express* 3 (2017), 025005, <https://doi.org/10.1088/2057-1976/aa5ccb>.
- [114] Z.F. Rad, R.E. Nordon, C.J. Anthony, L. Bilston, P.D. Prewett, J.Y. Arns, C.H. Arns, L. Zhang, G.J. Davies, High-fidelity replication of thermoplastic microneedles with open microfluidic channels, *Microsyst Nanoeng* 3 (2017) 1–11, <https://doi.org/10.1038/micronano.2017.34>.
- [115] S.W. Lee, S.S. Lee, Shrinkage ratio of PDMS and its alignment method for the wafer level process, *Microsyst. Technol.* 14 (2007) 205–208, <https://doi.org/10.1007/s00542-007-0417-y>.
- [116] R. Holmes, X.-B. Yang, A. Dunne, L. Florea, D. Wood, G. Tronci, Thiol-ene photoclick collagen-PEG hydrogels: impact of water-soluble photoinitiators on cell viability, gelation kinetics and rheological properties, *Polymers* 9 (2017) 226, <https://doi.org/10.3390/polym9060226>.
- [117] G. Palmara, F. Frascella, I. Roppolo, A. Chiappone, A. Chiadò, Functional 3D printing: approaches and bioapplications, *Biosens. Bioelectron.* 175 (2021), 112849, <https://doi.org/10.1016/j.bios.2020.112849>.
- [118] Q. Yang, W. Zhong, L. Xu, H. Li, Q. Yan, Y. She, G. Yang, Recent progress of 3D-printed microneedles for transdermal drug delivery, *Int. J. Pharm.* 593 (2021), 120106, <https://doi.org/10.1016/j.ijpharm.2020.120106>.
- [119] J. Arya, S. Henry, H. Kalluri, D.V. McAllister, W.P. Pewin, M.R. Prausnitz, Tolerability, usability and acceptability of dissolving microneedle patch administration in human subjects, *Biomaterials* 128 (2017) 1–7, <https://doi.org/10.1016/j.biomaterials.2017.02.040>.
- [120] D.D. Zhu, X.P. Zhang, B.L. Zhang, Y.Y. Hao, X.D. Guo, Safety assessment of microneedle technology for transdermal drug delivery: a review, *Adv. Ther.* 3 (2020) 1–14, <https://doi.org/10.1002/adtp.202000033>.
- [121] T. Sheng, B. Luo, W. Zhang, X. Ge, J. Yu, Y. Zhang, Z. Gu, Microneedle-mediated vaccination: innovation and translation, *Adv. Drug Deliv. Rev.* 179 (2021), 113919, <https://doi.org/10.1016/j.addr.2021.113919>.
- [122] T. Waghule, G. Singhvi, S.K. Dubey, M.M. Pandey, G. Gupta, M. Singh, K. Dua, Microneedles: a smart approach and increasing potential for transdermal drug delivery system, *Biomed. Pharmacother.* 109 (2019) 1249–1258, <https://doi.org/10.1016/j.biopha.2018.10.078>.
- [123] A. Muheem, F. Shakeel, M.A. Jahangir, M. Anwar, N. Mallick, G.K. Jain, M. H. Warsi, F.J. Ahmad, A review on the strategies for oral delivery of proteins and peptides and their clinical perspectives, *Saudi Pharmaceut. J.* 24 (2016) 413–428, <https://doi.org/10.1016/j.jsps.2014.06.004>.
- [124] A.J. Guillot, A.S. Cordeiro, R.F. Donnelly, M.C. Montesinos, T.M. Garrigues, A. Melero, Microneedle-based delivery: an overview of current applications and trends, *Pharmaceutics* 12 (2020) 569, <https://doi.org/10.3390/pharmaceutics12060569>.
- [125] K. Moussi, A.A. Haneef, R.A. Alsiary, E.M. Diallo, M.A. Boone, H. Abu-Araki, O. O. Al-Radi, J. Kosel, A microneedles balloon catheter for endovascular drug delivery, *Adv. Mater. Technol.* 6 (2021), <https://doi.org/10.1002/admt.202100037>.
- [126] Z. Chen, H. Wu, S. Zhao, X. Chen, T. Wei, H. Peng, Z. Chen, 3D-Printed integrated ultrasonic microneedle array for rapid transdermal drug delivery, *Mol. Pharm.* 19 (2022) 3314–3322, <https://doi.org/10.1021/acs.molpharmaceut.2c00466>.
- [127] H. Erkus, T. Bedir, E. Kaya, G.B. Tinaz, O. Gunduz, M.-C. Chifriuc, C.B. Ustundag, Innovative transdermal drug delivery system based on amoxicillin-loaded gelatin methacryloyl microneedles obtained by 3D printing, *Materialia (Oxf)* 27 (2023), 101700, <https://doi.org/10.1016/j.mta.2023.101700>.
- [128] X. Zhang, Y. Wang, J. Chi, Y. Zhao, Smart microneedles for therapy and diagnosis, *Research (2020)* 2020, <https://doi.org/10.34133/2020/7462915>.
- [129] S.D. Gittard, P.R. Miller, C. Jin, T.N. Martin, R.D. Boehm, B.J. Chisholm, S. J. Stafsljen, J.W. Daniels, N. Cilz, N.A. Monteiro-Riviere, A. Nasir, R.J. Narayan, Deposition of antimicrobial coatings on microstereolithography-fabricated microneedles, *Jom* 63 (2011) 59–68, <https://doi.org/10.1007/s11837-011-0093-3>.
- [130] M. Samandari, F. Aghabaglou, K. Nuutila, H. Derakhshandeh, Y. Zhang, Y. Endo, S. Harris, L. Barnum, C. Kreikemeier-Bower, E. Arab-Tehrany, N.A. Peppas, I. Sinha, A. Tamayol, Miniaturized needle array-mediated drug delivery accelerates wound healing, *Adv. Healthcare Mater.* 10 (2021), <https://doi.org/10.1002/adhm.202001800>.
- [131] J.J. Tomasek, G. Gabbiani, B. Hinz, C. Chaponnier, R.A. Brown, Myofibroblasts and mechano-regulation of connective tissue remodelling, *Nat. Rev. Mol. Cell Biol.* 3 (2002) 349–363, <https://doi.org/10.1038/nrm809>.
- [132] J.R. Sharpe, Y. Martin, Strategies demonstrating efficacy in reducing wound contraction in vivo, *Adv. Wound Care* 2 (2013) 167–175, <https://doi.org/10.1089/wound.2012.0378>.
- [133] A.R. Johnson, C.L. Caudill, J.R. Tumbleston, C.J. Bloomquist, K.A. Moga, A. Ermoshkin, D. Shirvanyants, S.J. Mechem, J.C. Luft, J.M. De Simone, Single-step fabrication of computationally designed microneedles by continuous liquid interface production, *PLoS One* 11 (2016) 1–17, <https://doi.org/10.1371/journal.pone.0162518>.
- [134] M. Yin, L. Xiao, Q. Liu, S.Y. Kwon, Y. Zhang, P.R. Sharma, L. Jin, X. Li, B. Xu, 3D printed microheater sensor-integrated, drug-encapsulated microneedle patch system for pain management, *Adv. Healthcare Mater.* 8 (2019) 1–10, <https://doi.org/10.1002/adhm.201901170>.
- [135] M. Friedel, I.A.P. Thompson, G. Kasting, R. Polsky, D. Cunningham, H.T. Soh, J. Heikenfeld, Opportunities and challenges in the diagnostic utility of dermal interstitial fluid, *Nat. Biomed. Eng.* (2023), <https://doi.org/10.1038/s41551-022-00998-9>.
- [136] N. Xu, W. Xu, M. Zhang, J. Yu, G. Ling, P. Zhang, Microneedle-based technology: toward minimally invasive disease diagnostics, *Adv. Mater. Technol.* 7 (2022) 1–19, <https://doi.org/10.1002/admt.202101595>.
- [137] P. Xue, L. Zhang, Z. Xu, J. Yan, Z. Gu, Y. Kang, Blood sampling using microneedles as a minimally invasive platform for biomedical diagnostics, *Appl. Mater. Today* 13 (2018) 144–157, <https://doi.org/10.1016/j.apmt.2018.08.013>.
- [138] M.M. Niedzwiecki, P. Samant, D.I. Walker, V. Tran, D.P. Jones, M.R. Prausnitz, G. W. Miller, Human suction blister fluid composition determined using high-resolution metabolomics, *Anal. Chem.* 90 (2018) 3786–3792, <https://doi.org/10.1021/acs.analchem.7b04073>.
- [139] A.C. Müller, F.P. Breitwieser, H. Fischer, C. Schuster, O. Brandt, J. Colinge, G. Superti-Furga, G. Stingl, A. Elbe-Bürger, K.L. Bennett, A comparative proteomic study of human skin suction blister fluid from healthy individuals using immunodepletion and iTRAQ labeling, *J. Proteome Res.* 11 (2012) 3715–3727, <https://doi.org/10.1021/pr3002035>.
- [140] S. Kayashima, T. Arai, M. Kikuchi, N. Nagata, N. Ito, T. Kuriyama, J. Kimura, Suction effusion fluid from skin and constituent analysis: new candidate for interstitial fluid, *Am. J. Physiol. Heart Circ. Physiol.* 263 (1992) H1623–H1627, <https://doi.org/10.1152/ajpheart.1992.263.5.H1623>.
- [141] A. Sieg, R.H. Guy, M. Begoña Delgado-Charro, Electroosmosis in transdermal iontophoresis: implications for noninvasive and calibration-free glucose monitoring, *Biophys. J.* 87 (2004) 3344–3350, <https://doi.org/10.1529/biophysj.104.044792>.
- [142] A.L. Krogstad, P.A. Jansson, P. Gisslén, P. Lönnroth, Microdialysis methodology for the measurement of dermal interstitial fluid in humans, *Br. J. Dermatol.* 134 (1996) 1005–1012.
- [143] M. Bodenlenz, K.I. Tiffner, R. Raml, T. Augustin, C. Dragatin, T. Birngruber, D. Schimek, G. Schwagerle, T.R. Pieber, S.G. Raney, I. Kanfer, F. Sinner, Open flow microperfusion as a dermal pharmacokinetic approach to evaluate topical bioequivalence, *Clin. Pharmacokinet.* 56 (2017) 91–98, <https://doi.org/10.1007/s40262-016-0442-z>.
- [144] M. Zheng, Z. Wang, H. Chang, L. Wang, S.W.T. Chew, D.C.S. Lio, M. Cui, L. Liu, B. C.K. Tee, C. Xu, Osmosis-powered hydrogel microneedles for microliters of skin interstitial fluid extraction within minutes, *Adv. Healthcare Mater.* 9 (2020), 1901683, <https://doi.org/10.1002/adhm.201901683>.
- [145] A. Mandal, A.V. Boopathy, L.K.W. Lam, K.D. Moynihan, M.E. Welch, N. R. Bennett, M.E. Turvey, N. Thai, V.H. Jenny, J.C. Love, P.T. Hammond, D. J. Irvine, Cell and fluid sampling microneedle patches for monitoring skin-resident immunity, *Sci. Transl. Med.* 10 (2018), <https://doi.org/10.1126/scitranslmed.aar2227>.
- [146] P.R. Miller, R.M. Taylor, B.Q. Tran, G. Boyd, T. Glaros, V.H. Chavez, R. Krishnakumar, A. Sinha, K. Poorey, K.P. Williams, S.S. Branda, J.T. Baca, R. Polsky, Extraction and biomolecular analysis of dermal interstitial fluid collected with hollow microneedles, *Commun. Biol.* 1 (2018), <https://doi.org/10.1038/s42003-018-0170-z>.
- [147] P.P. Samant, M.M. Niedzwiecki, N. Raviele, V. Tran, J. Mena-Lapaix, D.I. Walker, E.I. Felner, D.P. Jones, G.W. Miller, M.R. Prausnitz, Sampling interstitial fluid from human skin using a microneedle patch, *Sci. Transl. Med.* 12 (2020) 1–16, <https://doi.org/10.1126/SCITRANSLMED.AAW0285>.
- [148] J.G. Turner, E. Lay, U. Jungwirth, V. Varenko, H.S. Gill, P. Estrela, H.S. Leese, 3D-Printed hollow microneedle-lateral flow devices for rapid blood-free detection of C-reactive protein and prolactin, *Adv. Mater. Technol.* 2300259 (2023) 1–12, <https://doi.org/10.1002/admt.202300259>.
- [149] K. Liang, C. Leong, J.M. Loh, N. Chan, L. Lim, Y.I. Lam, T.L. Dawson, H.L. Tey, A 3D-printed transepidermal microprojection array for human skin microbiome sampling, *Proc. Natl. Acad. Sci. USA* 119 (2022), <https://doi.org/10.1073/pnas.2203556119>.
- [150] X. Qiu, J. De Jesus, M. Pennell, M. Troiani, J.B. Haun, Microfluidic device for mechanical dissociation of cancer cell aggregates into single cells, *Lab Chip* 15 (2015) 339–350, <https://doi.org/10.1039/C4LC01126K>.
- [151] M. Tahara, T. Inoue, Y. Miyakura, H. Horie, Y. Yasuda, H. Fujii, K. Kotake, K. Sugano, Cell diameter measurements obtained with a handheld cell counter could be used as a surrogate marker of G2/M arrest and apoptosis in colon cancer cell lines exposed to SN-38, *Biochem. Biophys. Res. Commun.* 434 (2013) 753–759, <https://doi.org/10.1016/j.bbrc.2013.03.128>.
- [152] J. Madden, C. O'Mahony, M. Thompson, A. O'Riordan, P. Galvin, Biosensing in dermal interstitial fluid using microneedle based electrochemical devices, *Sens Biosensing Res.* 29 (2020), 100348, <https://doi.org/10.1016/j.sbsr.2020.100348>.
- [153] G.S. Liu, Y. Kong, Y. Wang, Y. Luo, X. Fan, X. Xie, B.R. Yang, M.X. Wu, Microneedles for transdermal diagnostics: recent advances and new horizons, *Biomaterials* (2020) 232, <https://doi.org/10.1016/j.biomaterials.2019.119740>.
- [154] B. Ciui, A. Martin, R.K. Mishra, B. Brunetti, T. Nakagawa, T.J. Dawkins, M. Lyu, C. Cristea, R. Sandulescu, J. Wang, Wearable wireless tyrosinase bandage and microneedle sensors: toward melanoma screening, *Adv. Healthcare Mater.* 7 (2018) 1–9, <https://doi.org/10.1002/adhm.201701264>.
- [155] P.R. Miller, X. Xiao, I. Brener, D.B. Burckel, R. Narayan, R. Polsky, Microneedle-based transdermal sensor for on-chip potentiometric determination of K⁺, *Adv. Healthcare Mater.* 3 (2014) 876–881, <https://doi.org/10.1002/adhm.201300541>.
- [156] X. Zhang, G. Chen, F. Bian, L. Cai, Y. Zhao, Encoded microneedle arrays for detection of skin interstitial fluid biomarkers, *Adv. Mater.* 31 (2019) 1–8, <https://doi.org/10.1002/adma.201902825>.

- [157] T.M. Rawson, S.A.N. Gowers, D.M.E. Freeman, R.C. Wilson, S. Sharma, M. Gilchrist, A. MacGowan, A. Lovering, M. Bayliss, M. Kyriakides, P. Georgiou, A.E.G. Cass, D. O'Hare, A.H. Holmes, Microneedle biosensors for real-time, minimally invasive drug monitoring of phenoxymethylpenicillin: a first-in-human evaluation in healthy volunteers, *Lancet Digit Health* 1 (2019) e335–e343, [https://doi.org/10.1016/S2589-7500\(19\)30131-1](https://doi.org/10.1016/S2589-7500(19)30131-1).
- [158] F. Tehrani, H. Teymourian, B. Wuerstle, J. Kavner, R. Patel, A. Furnidge, R. Aghavali, H. Hosseini-Toudeshki, C. Brown, F. Zhang, K. Mahato, Z. Li, A. Barfidokht, L. Yin, P. Warren, N. Huang, Z. Patel, P.P. Mercier, J. Wang, An integrated wearable microneedle array for the continuous monitoring of multiple biomarkers in interstitial fluid, *Nat. Biomed. Eng.* 6 (2022) 1214–1224, <https://doi.org/10.1038/s41551-022-00887-1>.
- [159] F. Li, J. Ye, M. Zhou, S. Gan, Q. Zhang, D. Han, L. Niu, All-solid-state potassium-selective electrode using graphene as the solid contact, *Analyst* 137 (2012) 618–623, <https://doi.org/10.1039/C1AN15705A>.
- [160] Y. Liu, Q. Yu, X. Luo, L. Yang, Y. Cui, Continuous monitoring of diabetes with an integrated microneedle biosensing device through 3D printing, *Microsyst Nanoeng* 7 (2021), <https://doi.org/10.1038/s41378-021-00302-w>.
- [161] U. Detamornrat, E. McAlister, A.R.J. Hutton, E. Larraneta, R.F. Donnelly, The role of 3D printing technology in microengineering of microneedles, *Small* 18 (2022), 2106392, <https://doi.org/10.1002/sml.202106392>.
- [162] A. Nanda, Cancer Survivor Gets 3D-Printed Prosthetic Nose from Tan Tock Seng Hospital, *The Straits Times*, 2023.
- [163] H. Zhu, J. Mah Jian Qiang, C.G. Wang, C.Y. Chan, Q. Zhu, E. Ye, Z. Li, X.J. Loh, Flexible polymeric patch based nanotherapeutics against non-cancer therapy, *Bioact. Mater.* 18 (2022) 471–491, <https://doi.org/10.1016/j.bioactmat.2022.03.034>.
- [164] N. Elahpour, F. Pahlevanzadeh, M. Kharaziha, H.R. Bakhsheshi-Rad, S. Ramakrishna, F. Berto, 3D printed microneedles for transdermal drug delivery: a brief review of two decades, *Int. J. Pharm.* 597 (2021), 120301, <https://doi.org/10.1016/j.ijpharm.2021.120301>.
- [165] A. Than, C. Liu, H. Chang, P.K. Duong, C.M.G. Cheung, C. Xu, X. Wang, P. Chen, Self-implantable double-layered micro-drug-reservoirs for efficient and controlled ocular drug delivery, *Nat. Commun.* 9 (2018) 1–12, <https://doi.org/10.1038/s41467-018-06981-w>.
- [166] M. Amer, R.K. Chen, Self-Adhesive microneedles with interlocking features for sustained ocular drug delivery, *Macromol. Biosci.* 20 (2020), 2000089, <https://doi.org/10.1002/mabi.202000089>.
- [167] Y.C. Kim, H.E. Grossniklaus, H.F. Edelhauser, M.R. Prausnitz, Intrastromal delivery of bevacizumab using microneedles to treat corneal neovascularization, *Investigative Ophthalmol. Vis. Sci.* 55 (2014) 7376, <https://doi.org/10.1167/iov.14-15257>.
- [168] J. Lee, E.H. Jang, J.H. Kim, S. Park, Y. Kang, S. Park, K. Lee, J.-H. Kim, Y.-N. Youn, W. Ryu, Highly flexible and porous silk fibroin microneedle wraps for perivascular drug delivery, *J. Contr. Release* 340 (2021) 125–135, <https://doi.org/10.1016/j.jconrel.2021.10.024>.
- [169] B. Mbituyimana, G. Ma, Z. Shi, G. Yang, Polymer-based microneedle composites for enhanced non-transdermal drug delivery, *Appl. Mater. Today* 29 (2022), 101659, <https://doi.org/10.1016/j.apmt.2022.101659>.
- [170] R.L. Creighton, K.A. Woodrow, Microneedle-mediated vaccine delivery to the oral mucosa, *Adv. Healthcare Mater.* 176 (2018), 1801180, <https://doi.org/10.1002/adhm.201801180>.
- [171] S. Lim, T.Y. Park, E.Y. Jeon, K. Il Joo, H.J. Cha, Double-layered adhesive microneedle bandage based on biofunctionalized mussel protein for cardiac tissue regeneration, *Biomaterials* 278 (2021), 121171, <https://doi.org/10.1016/j.biomaterials.2021.121171>.
- [172] P. Wang, J. Wu, H. Yang, H. Liu, T. Yao, C. Liu, Y. Gong, M. Wang, G. Ji, P. Huang, X. Wang, Intelligent microneedle patch with prolonged local release of hydrogen and magnesium ions for diabetic wound healing, *Bioact. Mater.* 24 (2023) 463–476, <https://doi.org/10.1016/j.bioactmat.2023.01.001>.
- [173] N. Wang, Y. Zhen, Y. Jin, X. Wang, N. Li, S. Jiang, T. Wang, Combining different types of multifunctional liposomes loaded with ammonium bicarbonate to fabricate microneedle arrays as a vaginal mucosal vaccine adjuvant-dual delivery system (VADDS), *J. Contr. Release* 246 (2017) 12–29, <https://doi.org/10.1016/j.jconrel.2016.12.009>.
- [174] S.P. Sullivan, D.G. Koutsonanos, M. del Pilar Martin, J.W. Lee, V. Zarnitsyn, S.-O. Choi, N. Murthy, R.W. Compans, I. Skountzou, M.R. Prausnitz, Dissolving polymer microneedle patches for influenza vaccination, *Nat. Med.* 16 (2010) 915–920, <https://doi.org/10.1038/nm.2182>.
- [175] M. Kirkby, A.R.J. Hutton, R.F. Donnelly, Microneedle mediated transdermal delivery of protein, peptide and antibody based therapeutics: current status and future considerations, *Pharm. Res. (N. Y.)* 37 (2020) 1–18, <https://doi.org/10.1007/s11095-020-02844-6>.
- [176] Z. Zhang, W. Li, D. Chang, Z. Wei, E. Wang, J. Yu, Y. Xu, Y. Que, Y. Chen, C. Fan, B. Ma, Y. Zhou, Z. Huan, C. Yang, F. Guo, J. Chang, A combination therapy for androgenic alopecia based on quercetin and zinc/copper dual-doped mesoporous silica nanocomposite microneedle patch, *Bioact. Mater.* 24 (2023) 81–95, <https://doi.org/10.1016/j.bioactmat.2022.12.007>.
- [177] L.L. Lin, T.W. Prow, A.P. Raphael, R.L. Harrold III, C.A. Primiero, A.B. Ansaldo, H. P. Soyer, Microbiopsy engineered for minimally invasive and suture-free sub-millimetre skin sampling, *F1000Res* 2 (2013) 120, <https://doi.org/10.12688/f1000research.2-120.v2>.
- [178] Data Bridge Market Research, Global Microneedle Drug Delivery Systems Market – Industry Trends and Forecast to 2027, 2020.
- [179] Center for Devices and Radiological Health, Guidance Document: Regulatory Considerations for Microneedling Products, United States of America, 2020.
- [180] D. of H. and H.S. Food and Drug Administration, 21 CFR Part 820, 61 FR 52654, Oct. 7, 1996, unless Otherwise Noted, United States of America, 1996.
- [181] Q. management and corresponding general aspects for medical devices, Technical Committee ISO/TC 210, ISO 13485:2016 Medical devices — quality management systems — Requirements for regulatory purposes. <https://www.iso.org/standard/59752.html>, 2016.
- [182] Center for Devices and Radiological Health, Guidance document: technical considerations for additive manufactured medical devices. <https://www.fda.gov/regulatory-information/search-fda-guidance-documents/technical-considerations-additive-manufactured-medical-devices>, 2017. United States of America.